

Online Appendix C of  
**Distribution of REE between amphibole and pyroxenes in the  
lithospheric mantle: An assessment from the lattice strain model**

Chunguang Wang<sup>1,\*</sup>, Yan Liang<sup>2</sup>, Wenliang Xu<sup>1</sup>, Chenguang Sun<sup>3</sup>, and Kei Shimizu<sup>4</sup>

1. College of Earth Sciences, Jilin University, Changchun 130061, China
2. Department of Earth, Environmental and Planetary Sciences, Brown University, Providence, RI 02192, USA
3. Department of Geological Sciences, Jackson School of Geosciences, University of Texas at Austin, Austin, TX 78712, USA
4. WiscSIMS, Department of Geoscience, University of Wisconsin–Madison, Madison, WI 53706, USA

\*Corresponding author, E-mail: c\_wang@jlu.edu.cn

---

**Table of Contents**

<b>Text S1.</b>	Petrologic features of the amphibole-bearing mantle samples	1
<b>Table S1.</b>	Summary of textural and mineral chemical features for the amphibole-bearing mantle samples	3
<b>Text S2.</b>	Procedure of the amphibole formula calculation	4
<b>Table S2.</b>	An example of amphibole formular calculation using the procedure of Shimizu et al. (2017)	5
<b>Text S3.</b>	Tests of the pyroxene-amphibole REE partitioning models on peridotites from Eifel	6
<b>Table S3.</b>	Mineral Mg#s and temperatures of the amphibole-bearing peridotites from Eifel	6
<b>Figure S1–24.</b>	Inversion diagrams for $T_{\text{REE}}$ and $T^{\text{amp}}$	10
<b>References</b>		35

---

## **Text S1. Petrologic features of the amphibole-bearing mantle samples**

In this text, we describe textures and mineral compositions for the 28 amphibole-bearing mantle samples from literature with mineral compositions within the calibration ranges of the mineral-melt REE partitioning models. The key textural and mineral compositional features are listed in [Table S1](#). Based on these petrologic features, we check if amphibole and pyroxenes in each sample formed from the same metasomatic event. This procedure help filter out 4 samples that are not suitable for testing and calibrating the amphibole-pyroxene REE partitioning models in this study.

### **Lherzolites, harzburgites, and websterite from Western Pannonian Basin**

Twenty samples are from Western Pannonian Basin, Hungary, reported in Aradi et al. (2020). They are mostly lherzolites with coarse-grained protogranular and porphyroclastic textures. Amphibole occurs at rims of clinopyroxenes and spinels, and sometimes in veins. An olivine websterite (sample BEI1401) has a texture similar to the lherzolites. Two harzburgites (samples BF1411 and TOB1405) are phlogopite-bearing. Sample BF1411 has amphiboles replacing orthopyroxenes and clinopyroxenes, and the pyroxenes are partially recrystallized into euhedral or patchwork-structured amphiboles. Sample TOB1405 have primary pyroxene grains, whereas abundant (5.7%) secondary amphiboles form nets surrounding the primary grains. Sample RGB1456 has a sheared amphibole-bearing zone. Orthopyroxenes and clinopyroxenes in these samples have similar Mg#s. Amphibole Mg#s are 1.0–3.0 units lower than pyroxene Mg#s except TOB1405 and RGB1456 which have differences of 6.6/7.6 and 3.5/3.0 units between pyroxene Mg#s and amphibole Mg#. These two samples are excluded from the test and calibration.

### **Lherzolites from Nyos Lake**

Two lherzolites from Nyos Lake, Cameroon, reported by Pintér et al. (2015) have porphyroclastic textures. Amphibole exists interstitial to pyroxenes that have melted grain boundaries and fluid inclusions. Amphibole and pyroxenes are chemically uniform within each sample. Orthopyroxenes and clinopyroxenes have similar Mg#s, and are 2.3–3.0 units higher than amphibole Mg#s.

### **Lherzolite and wehrlite from Wilcza Góra**

One lherzolite and one wehrlite from Wilcza Góra, southwestern Poland, studied by Matusiak-Malek et al. (2017) have protogranular and equigranular textures. Irregular lenticular amphibole and clinopyroxene growth inside orthopyroxene grains in the lherzolite. Amphibole is overgrown by clinopyroxenes or form clusters with pyroxenes, olivine, spinel, and feldspar/glass in the wehrlite. Orthopyroxenes and clinopyroxenes have similar Mg#, which are 1.8–3.0 units higher than amphibole Mg#s.

### **Harzburgite from Kerguelen archipelago**

One harzburgite from Kerguelen archipelago, Indian Ocean, reported by Gregoire et al. (2000) is phlogopite-bearing. It has a poikilitic texture. Clinopyroxene grains contain resorbed orthopyroxene. Amphibole occurs as rounded interstitial grains or as inclusions in phlogopite grains. Orthopyroxenes and clinopyroxenes have similar Mg#, which are 1.7 and 2.6 units higher than the amphibole Mg#, respectively.

### **Lherzolite from Huadian**

The lherzolite sample 17XJ6-3, from Huadian, northeastern China (W Xu, unpublished data), has a granoblastic texture. Amphibole and pyroxene grains form equiangular triple junctions. Orthopyroxenes and clinopyroxenes have similar Mg#, which are 1.9 and 1.6 units higher than the amphibole Mg#, respectively.

### **Websterites from Laiwu**

Two websterites 11LW-3 and LW9-16 from Laiwu, North China Craton, reported by Zhou (2014), are porphyroclastic in texture. Minerals are uneven distributed. Bunches of orthopyroxenes or resorbed orthopyroxene grains are surrounded by clinopyroxene bunches, and amphibole exists interstitial to pyroxenes. Clinopyroxene Mg# is 3.5–6.0 units higher than orthopyroxene Mg#. The discrepancy between pyroxene Mg# and amphibole Mg# can be up to 8. These two samples are excluded from the test and calibration, since the textural and mineral compositional disequilibrium.

**Table S1. Summary of textural and mineral chemical features for the amphibole-bearing mantle samples**

Sample	Lithology	Texture	Modal abundance (%)						Mg#			Difference in Mg#			Location & data source	Note
			Ol	Opx	Cpx	Sp	Amp	Phl	Opx	Cpx	Amp	Opx-Cpx	Opx-Amp	Cpx-Amp		
BF1411	Harz	Porph	68.00	11.00	5.00		15.94	0.06	89.2	89.5	86.4	-0.2	2.8	3.0	1	<b>Omitted</b>
TOB1405	Harz	Porph	50.00	19.00	3.00	4.50	5.65	17.85	89.8	90.7	83.1	-0.9	<b>6.6</b>	<b>7.6</b>	1	
AUB1407	Lher	Prot	68.18	18.05	11.03	2.51	0.24		89.8	89.4	87.8	0.4	2.0	1.6	1	
AUB1410	Lher	Prot	58.36	26.16	13.08	2.31	0.08		90.7	90.7	89.0	0.0	1.7	1.7	1	
BEI1404	Lher	Prot	68.86	17.96	11.98	1.20	Trace		90.4	90.8	88.5	-0.4	1.9	2.3	1	
FKG1402	Lher	Prot	60.76	24.30	14.18	0.30	0.46		89.1	89.4	87.1	-0.3	2.0	2.3	1	
GN1401	Lher	Porph	68.04	19.01	10.01	0.90	2.04		90.5	90.9	88.2	-0.4	2.3	2.7	1	
GN1402	Lher	Porph	60.88	24.95	11.98	2.20	Trace		90.3	90.0	87.6	0.3	2.7	2.4	1	
GN1406	Lher	Prot	60.16	23.06	14.04	2.31	0.44		90.6	90.1	88.2	0.4	2.3	1.9	1	
GN1411	Lher	Porph	74.39	17.85	5.95	0.89	0.91		90.6	90.9	87.9	-0.3	2.7	3.0	1	
GN1412	Lher	Porph	71.42	15.09	12.07	1.41	0.01		90.3	90.0	87.8	0.3	2.5	2.2	1	<b>Omitted</b>
NH1402	Lher	Porph	53.38	27.20	16.12	3.22	0.08		90.0	90.1	87.6	-0.2	2.4	2.5	1	
NH1408	Lher	Porph	69.48	19.85	9.93	0.69	0.05		90.8	91.0	88.2	-0.2	2.6	2.8	1	
RGB1416	Lher	Prot	61.88	18.96	17.96	0.90	0.30		89.8	89.9	87.5	-0.1	2.3	2.4	1	
RGB1454	Lher	Porph	59.49	24.20	11.09	0.60	4.62		90.3	90.1	87.4	0.2	2.9	2.7	1	
RGB1456	Lher	<b>Sheared</b>	62.82	21.94	10.97	0.90	3.37		90.1	89.5	86.6	0.6	<b>3.5</b>	3.0	1	
SBF1401	Lher	Porph	73.95	15.99	7.99	2.00	0.07		90.7	91.6	89.7	-0.9	1.0	1.9	1	
TOB1401	Lher	Porph	55.65	26.83	14.91	2.09	0.53		90.5	89.5	88.2	0.9	2.2	1.3	1	
TOB1403	Lher	Porph	72.91	8.10	9.11	1.11	8.76		89.2	88.7	86.2	0.5	3.0	2.5	1	
BEI1401	Web	Porph	34.67	39.77	21.42	1.63	2.51		90.1	89.3	87.4	0.8	2.7	1.9	1	
Nyos2	Lher	Porph	50.80	37.70	7.90	2.60	1.00		90.3	90.9	88.0	-0.6	2.3	2.9	2	<b>Omitted</b>
Nyos3	Lher	Porph	76.40	12.30	8.20	2.10	1.00		91.1	91.8	88.8	-0.6	2.3	3.0	2	
WLK30	Lher	Prot to Egg	81.00	13.00	6.00		Trace		90.6	91.0	88.8	-0.4	1.8	2.2	3	
MM110	Whr	Prot	82.00	2.00	12.00	2.00	2.00		89.2	90.4	87.3	-1.2	1.9	3.0	3	
OB-93-5	Harz	Poikilitic	74.00	21.60	3.50	0.20	0.30	0.40	91.9	91.0	89.3	0.9	2.6	1.7	4	
17XJ6-3	Lher	Granoblastic	62.00	21.00	14.00	1.00	2.00		90.1	90.4	88.4	-0.3	1.6	1.9	5	
11LW-3	Web	Porph		70.00	27.00		3.00		82.3	85.7	77.6	-3.5	<b>4.6</b>	<b>8.1</b>	6	
LW9-16	Web	Porph		64.00	32.00		4.00		77.2	83.3	77.8	-6.0	-0.6	<b>5.4</b>	6	

Porph: porphyroclastic; Prot: protogranular; Egg: equigranular.

Harz: harzburgite; Lher: lherzolite; Web: websterite; Whr: wehrlite.

Ol: olivine; Opx: orthopyroxene; Cpx: clinopyroxene; Sp: spinel; Amp: amphibole; Phl: phlogopite.

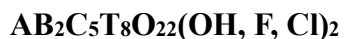
Sample locations and data sources are:

1. Western Pannonian Basin, Hungary (Aradi et al., 2020);
2. Nyos Lakes, Cameroon (Pinter et al., 2015);
3. Wilcza Góra, Southwestern Poland (Matusiak-Malek et al., 2017);
4. Huadian, northeastern China (Xu, unpublished);
5. Laiwu, North China Craton (Zhou, 2014).

## Text S2. Procedure of the amphibole formula calculation

Amphibole formula is calculated using the method of Shimizu et al. (2017). It is simplified from that described in Leake et al. (1997) by assuming all Fe to be ferrous.

The general chemical formula of amphiboles is:



where **A** = Na, K, or vacant in the A site; **B** = Ca, Na, Mn, Fe<sup>2+</sup>, Mg in the M4 sites; **C** = Fe<sup>2+</sup>, Fe<sup>3+</sup>, Mg, Al, Mn, Ti, Cr in the M1, M2, and M3 sites; **T** = Si, Al in the tetrahedral site (Hawthorne, 1983). In Table S2, we show the procedure by calculating the formula for amphibole in a hornblende from the Western Pannonian Basin (sample KPFS0402 from Aradi et al., 2020).

**Table S2. An example of amphibole formular calculation using the procedure of Shimizu et al. (2017)**

Row#		SiO <sub>2</sub>	TiO <sub>2</sub>	Al <sub>2</sub> O <sub>3</sub>	Cr <sub>2</sub> O <sub>3</sub>	FeOt	MnO	MgO	CaO	Na <sub>2</sub> O	K <sub>2</sub> O	Total
1	Oxides in wt%	Amphibole in sample KPFS0402 from the Western Pannonian Basin (Aradi et al., 2020)										
		42.57	1.38	14.45	1.02	4.30	0.08	18.44	11.19	3.62	0.02	97.06
2	Mole proportions	Row1 ÷ Oxide Molecular Weight										
		0.709	0.017	0.142	0.007	0.060	1.114×10 <sup>-3</sup>	0.457	0.200	0.058	2.176×10 <sup>-4</sup>	
3	Numbers of cations	Row2 × Cation Numbers Per Oxide										
		Si	Ti	Al	Cr	Fe	Mn	Mg	Ca	Na	K	
		0.709	0.017	0.283	0.013	0.060	1.114×10 <sup>-3</sup>	0.457	0.200	0.117	4.353×10 <sup>-4</sup>	
4	Numbers of O atoms	Row2 × O Atom Numbers Per Oxide										Total
		1.417	0.035	0.425	0.020	0.060	1.114×10 <sup>-3</sup>	0.457	0.200	0.058	2.176×10 <sup>-4</sup>	2.673
5	Numbers of cations per 23 O atoms	Row3 ÷ Total of Row4 × 23										
		Si	Ti	Al	Cr	Fe	Mn	Mg	Ca	Na	K	
		6.096	0.149	2.438	0.115	0.515	9.582×10 <sup>-3</sup>	3.936	1.717	1.005	3.745×10 <sup>-3</sup>	
6	Site occupancies	The T side accommodates Si, Al, and Ti, successively. The rest Al and/or Ti, if exist, are accommodated into the M1-3 (C) sites.				Fe, Mn, and Mg in the M1-3 (C) and M4 (B) sites.				Total Na in the A site and M4 (B) site and K in the A site.		
		<sup>T</sup> Si	<sup>T</sup> Ti	<sup>T</sup> Al	<sup>C</sup> Cr	Fe	Mn	Mg	<sup>B</sup> Ca	Na	K	
		6.096	0	1.904	0.115	0.515	9.582×10 <sup>-3</sup>	3.936	1.717	1.005	3.745×10 <sup>-3</sup>	
			<sup>C</sup> Ti	<sup>C</sup> Al		Fm = total Fe, Mn, Mg 4.460						
			0.149	0.534		<sup>C</sup> Fm = 5 - <sup>C</sup> Ti - <sup>C</sup> Al - <sup>C</sup> Cr 4.202						
						<sup>B</sup> Fm = Fm - <sup>C</sup> Fm 0.258						

The calculated components in bold are those used in the lattice strain model for amphibole-melt REE partitioning of Shimizu et al. (2017) [Eqs. (A1a and A1b) in Appendix A]:

$$X_{Ti} = Ti; X_{Mg} = Mg; X_{Na} = Na; X_K = K; X_{Fm}^{M4} = {}^B Fm.$$

### Text S3. Tests of the pyroxene-amphibole REE partitioning models on peridotites from Eifel

Witt-Eickschen and Harte (1994) and Eickschen and O'Neill (2005) reported petrology and mineral chemistry for 17 amphibole-bearing spinel lherzolite and harzburgite xenoliths from Eifel, western Germany (Table S3). We did not include these samples in the model calibrations due to their lower TiO<sub>2</sub> contents of amphiboles, falling outside the calibration range of the amphibole-melt REE partitioning model (Fig. ST1a; Shimizu et al., 2017). Additionally, only the 4 samples (from Witt-Eickschen and O'Neill, 2005) provide orthopyroxene REE data, leaving us without access to the T<sub>REEs</sub> for the remaining 13 samples (from Witt-Eickschen and Harte, 1994). Here we preform preliminary tests of our model on these samples.

**Table S3. Mineral Mg#s and temperatures of the amphibole-bearing peridotites from Eifel**

Sample	Mg#			Difference in Mg#		Temperatures (°C)			Data source
	Opx	Cpx	Amp	Opx-Amp	Cpx-Amp	T <sub>REE</sub>	T <sub>BKN</sub>	T <sup>amp</sup> (Eq. 8)	
<b>W110</b>	91.7	91.7	89.6	2.1	2.1	NA	<i>1010</i>	725	1
W194	91.6	91.4	89.3	2.3	2.1	NA	<i>1028</i>	806	1
W211	91.6	91.3	88.9	2.7	2.4	NA	<i>1003</i>	801	1
W766	91.7	90.9	89.5	2.1	1.4	NA	<i>1036</i>	763	1
W788	91.3	92.4	89.8	1.5	2.6	NA	<i>973</i>	817	1
W1262	91.3	90.8	88.7	2.6	2.1	NA	<i>1024</i>	794	1
<b>W1307</b>	91.5	91.6	86.9	4.6	<b>4.7</b>	NA	<b><i>1116</i></b>	<b>759</b>	1
W1310	91.8	90.5	89.5	2.3	1.0	NA	<i>929</i>	809	1
W1317	92.0	91.5	90.1	2.0	1.4	NA	<i>1072</i>	784	1
W1332	90.6	91.1	88.3	2.3	2.8	NA	<i>1022</i>	779	1
<b>E1157</b>	90.9	<b>94.1</b>	90.4	0.5	<b>3.7</b>	NA	<b>759</b>	<b>1047</b>	1
<b>E1160</b>	90.6	<b>93.6</b>	88.5	2.1	<b>5.1</b>	NA	<b>771</b>	<b>966</b>	1
<b>E1163</b>	91.4	<b>93.7</b>	89.1	2.4	<b>4.6</b>	NA	<b>913</b>	<b>937</b>	1
MM110	91.9	91.5	89.6	2.3	1.9	<i>959</i>	1014	725	2
MM766	91.9	92.1	89.5	2.4	2.5	<i>1015</i>	1026	763	2
MM1278	91.7	92.0	88.4	3.6	3.6	<i>947</i>	969	762	2
DW211	92.2	92.5	88.9	3.3	3.6	<i>907</i>	955	801	2

Opx: orthopyroxene; Cpx: clinopyroxene; Amp: amphibole; NA: not available.

T<sub>REE</sub>: temperature calculated using the REE-in-two-pyroxene thermometer of Liang et al. (2013).

T<sub>BKN</sub>: temperature calculated using the two-pyroxene thermometer of Brey and Köhler (1990), assuming a pressure of 1.5 GPa.

Samples in bold are those got unsatisfactory D<sup>cpx-amp</sup> predictions from the clinopyroxene-amphibole REE partitioning model.

Temperatures in italic are those used to represent the pyroxene temperature in the partitioning models.

Data sources are: 1. Witt-Eickschen and Harte (1994), 2. Witt-Eickschen and O'Neill (2005).

Amphiboles in the Eifel samples commonly exist as isolated interstitial grains that are in textural equilibrium with the other phases. The differences in Mg#s between pyroxene and amphibole are within 3.6 units (mostly within 2.8 units), except the following 4 samples. In sample W1307, amphiboles are present as poikilitic crystals enclosing clinopyroxenes. The orthopyroxene-amphibole and clinopyroxene-amphibole Mg#

differences are large (4.6 and 4.7 units, respectively, Table S3, Fig. ST1b). In samples E1157, E1160 and E1163, amphiboles mainly exist as polygonal neoblasts. Mg#s in clinopyroxene of these samples are high (93.6–94.1), which are 3.7–5.1 units higher than Mg#s in amphibole (Table S3, Fig. ST1b).

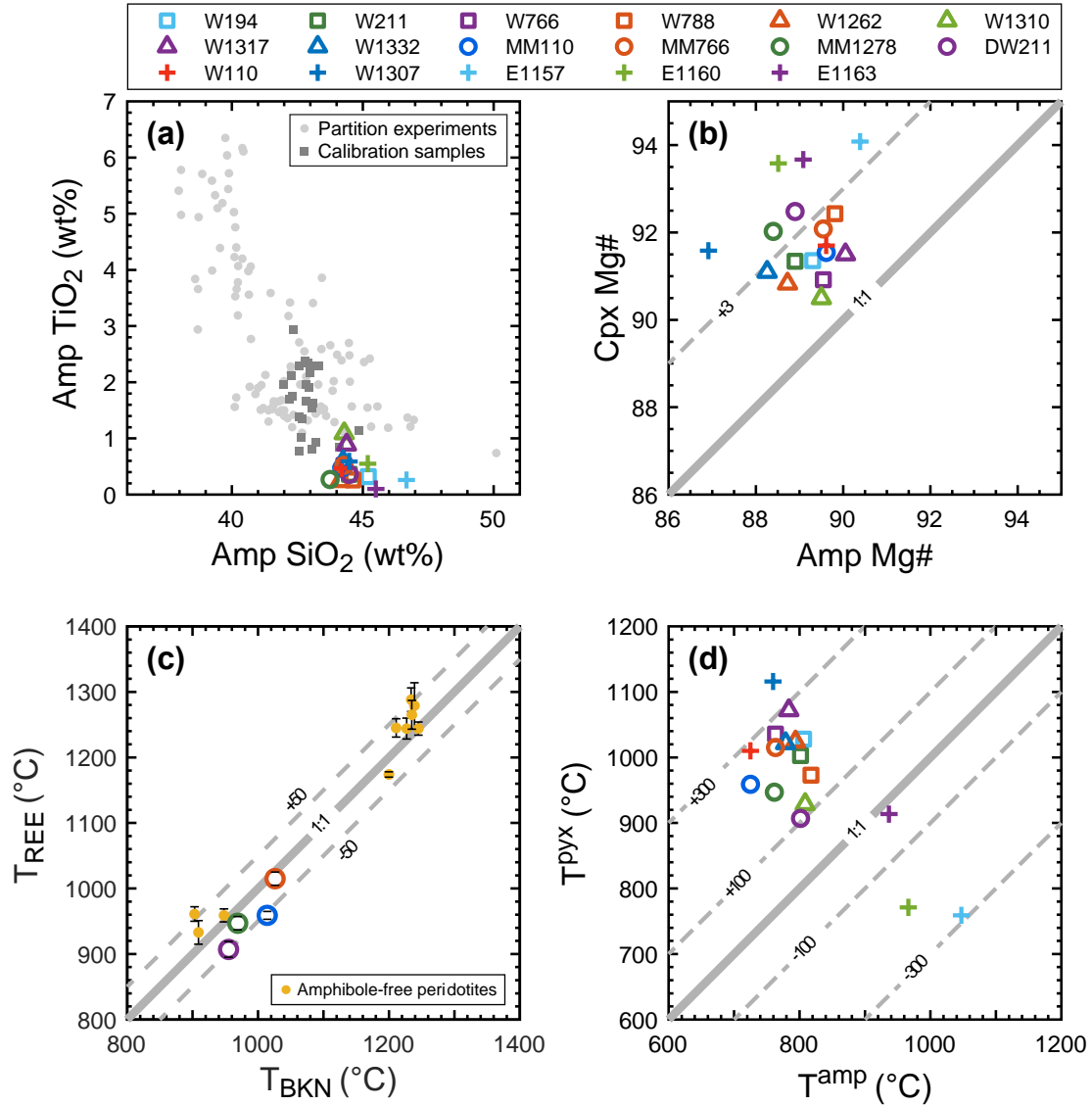


**Figure ST1.** Mineral compositions and temperatures of the peridotites from Eifel (Witt-Eickschen and Harte, 1994; Witt-Eickschen and O'Neill, 2005). **a.** Plot of TiO<sub>2</sub> content against SiO<sub>2</sub> content in amphiboles of the Eifel samples. Compositions of amphiboles from the amphibole–melt REE partitioning experiments used to calibrate the model of Shimizu et al. (2017) and amphiboles from the 24 natural samples used to calibrate the pyroxene–amphibole REE partitioning models are plotted for comparison. **b.** Comparisons of amphibole Mg# with clinopyroxene Mg#. **c.** Comparison of  $T_{REE}$  (Liang et al. 2013) with  $T_{BKN}$  (Brey and Köhler, 1990) for the amphibole-bearing and amphibole-free peridotites. **d.** Comparisons of the pyroxene temperature ( $T_{BKN}$  or  $T_{REE}$ , Table S3) with the  $T^{amp}$  calculated using Eq. (8).

Liang et al. (2013) calculated the two-pyroxene temperatures for the Eifel xenoliths from Witt-Eickschen and O'Neill (2005) including 4 amphibole-bearing peridotites (MM110, MM766, MM1278, and DW211).  $T_{\text{REES}}$  are similar to  $T_{\text{BKNS}}$  for both the amphibole-bearing and amphibole-free peridotites (Table S3, Fig. ST1c). This similarity provides us with confidence in utilizing  $T_{\text{BKN}}$  to represent  $T_{\text{Pyx}}$  in our partition models for the samples from Witt-Eickschen and Harte (1994) that lack accessible  $T_{\text{REE}}$ . Using Eq. (8), we calculated  $T^{\text{amp}}$ s for the 17 samples. Except for the samples displaying disequilibrium amphibole occurrences and Mg#s (W1307, E1157, E1160 and E1163),  $T_{\text{Pyx}}$ s are 100–300° C higher than  $T^{\text{amp}}$ s (Fig. ST1d).  $T_{\text{Pyx}}$  is 356°C higher than  $T^{\text{amp}}$  for sample W1307, whereas  $T_{\text{Pyx}}$ s are 23–288°C lower than  $T^{\text{amp}}$ s for samples E1157, E1160 and E1163 (Fig. ST1d).

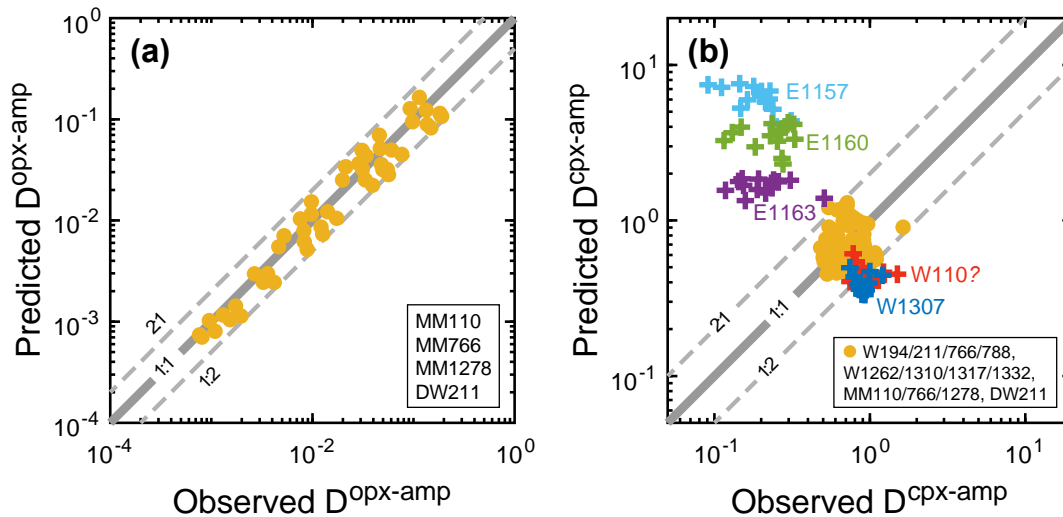


**Figure ST2.** Comparison between model-predicted and measured pyroxene-amphibole REE partition coefficients for the peridotites from Eifel (Witt-Eickschen and Harte, 1994; Witt-Eickschen and O'Neill, 2005).

Applying our models, we calculated pyroxene-amphibole REE partition coefficients for the Eifel samples and compared them with the measured values in Fig. ST2. The orthopyroxene-amphibole model yields good predictions of partition coefficients for the 4 samples with orthopyroxene REE data reported (Witt-Eickschen and O'Neill, 2005) (Fig. ST2a). The clinopyroxene-amphibole model is capable of reproducing partition coefficients for most samples, excluding W1307, E1157, E1160, E1163, and W110 (Fig. ST2b). Most of these exceptions exhibit disequilibrium texture and Mg#s, as detailed earlier. The model overestimated  $D^{\text{cpx-amp}}$ s for samples E1157, E1160, and E1163, which

have unusually lower  $T^{\text{pyxs}}$  than  $T^{\text{amps}}$  (Fig. ST1d). Conversely, it underestimated  $D^{\text{cpx-amps}}$  for sample W1307 which has a  $T^{\text{pyx}}$  significantly higher than  $T^{\text{amp}}$  (Fig. ST1d).

Through this set of preliminary application, we infer that the pyroxene-amphibole REE partition models presented in this study are effective in predicting REE partition coefficients for mantle rocks with amphibole compositions close to the calibration range of the amphibole-melt model of Shimizu et al. (2017). However, it is crucial to note that the success of these models depends on a close genetic link between amphibole and coexisting pyroxenes in terms of texture and mineral chemistry. We also suggest that the compositional range of application for these models could potentially be expanded providing calibrations against additional partitioning experiments and natural amphibole-bearing samples.

## Figure S1–24. Inversion diagrams for $T_{\text{REE}}$ and $T^{\text{amp}}$

- a. Inversion diagram for  $T_{\text{REE}}$  using the REE-in-two-pyroxene thermometer of Liang et al. (2013).
- b. Comparison of the measured clinopyroxene-orthopyroxene REE partition coefficients (red pattern) with those calculated using the clinopyroxene-orthopyroxene REE partition model of Liang et al. (2013) at the inverted  $T_{\text{REE}}$  (solid blue curve).
- c. Inversion diagram of apparent amphibole temperature ( $T^{\text{amp,opx-amp}}$ ) using the semi-empirical model of Eq. (5).
- d. Comparison of the measured orthopyroxene-amphibole REE partition coefficients (red pattern) with those calculated using the REE partitioning model with pyroxene temperature at  $T_{\text{REE}}$  and amphibole temperature at the inverted  $T^{\text{amp,opx-amp}}$  (solid green curve).
- e. Inversion diagram of apparent amphibole temperature ( $T^{\text{amp,cpx-amp}}$ ) using the semi-empirical model of Eq. (5).
- f. Comparison of the measured clinopyroxene-amphibole REE partition coefficients (red pattern) with those calculated using the REE partitioning model with pyroxene temperature at  $T_{\text{REE}}$  and amphibole temperature the inverted  $T^{\text{amp,cpx-amp}}$  (solid green curve).

Gray circles in the inversion diagrams in (a, c, and e) are data manually excluded from the robust linear least-squares regression (thick blue or green line). Pyroxene-amphibole REE partition coefficients calculated assuming  $T^{\text{amp}} = T_{\text{REE}}$  (upper),  $T_{\text{REE}} - 100^{\circ}\text{C}$  (middle), and  $T_{\text{REE}} - 200^{\circ}\text{C}$  (lower) were plotted as dot-dashed green isothermal curves in (d and f) for comparison.

Fig. S1. OB-93-5, Kerguelen archipelago, Indian Ocean, Gregoire et al. (2000)

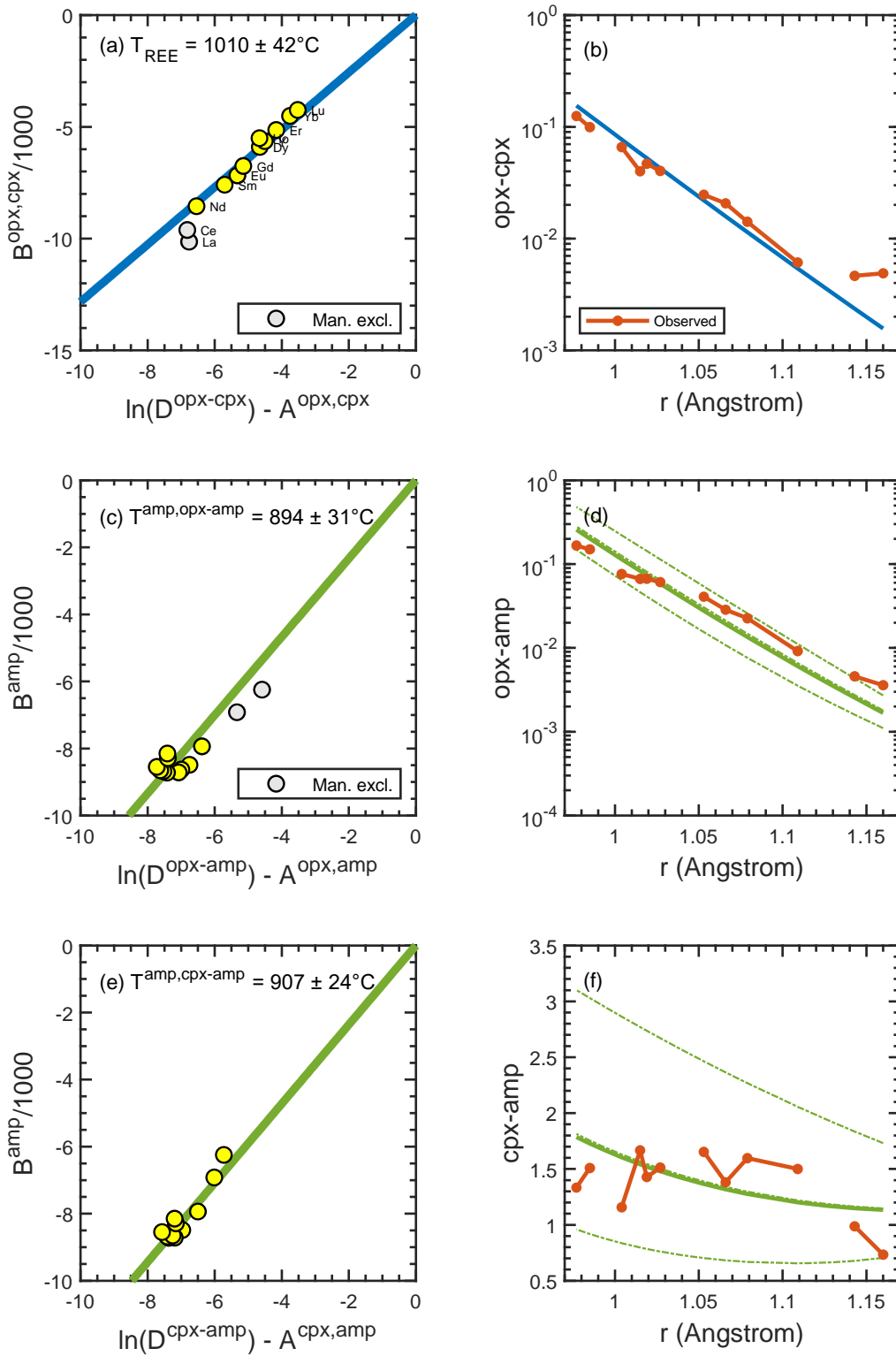


Fig. S2. BF1411, Western Pannonian Basin, Hungary, Aradi et al. (2020)

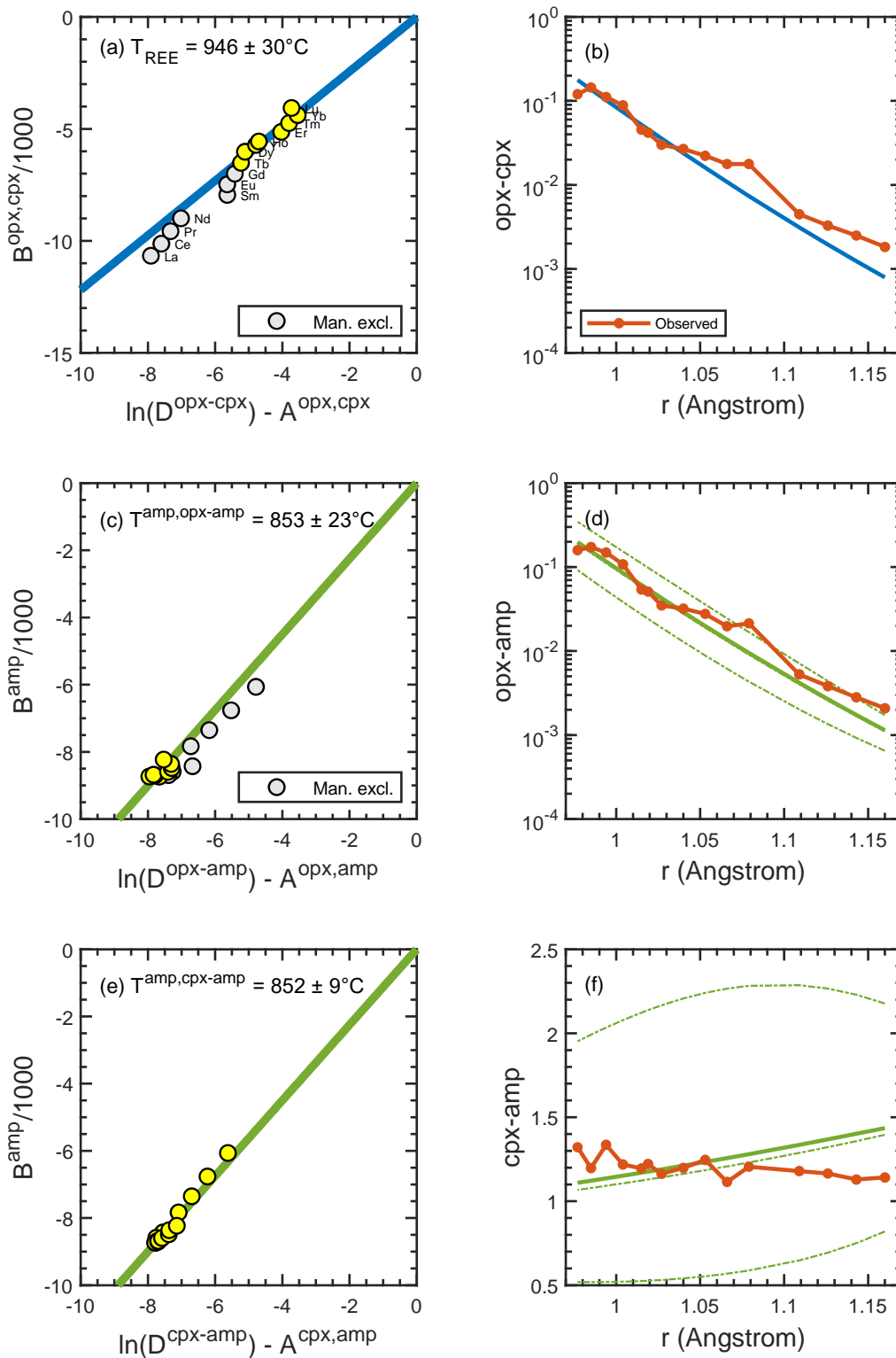


Fig. S3. Nyos2, Nyos Lakes, Cameroon, Pinter et al. (2015)

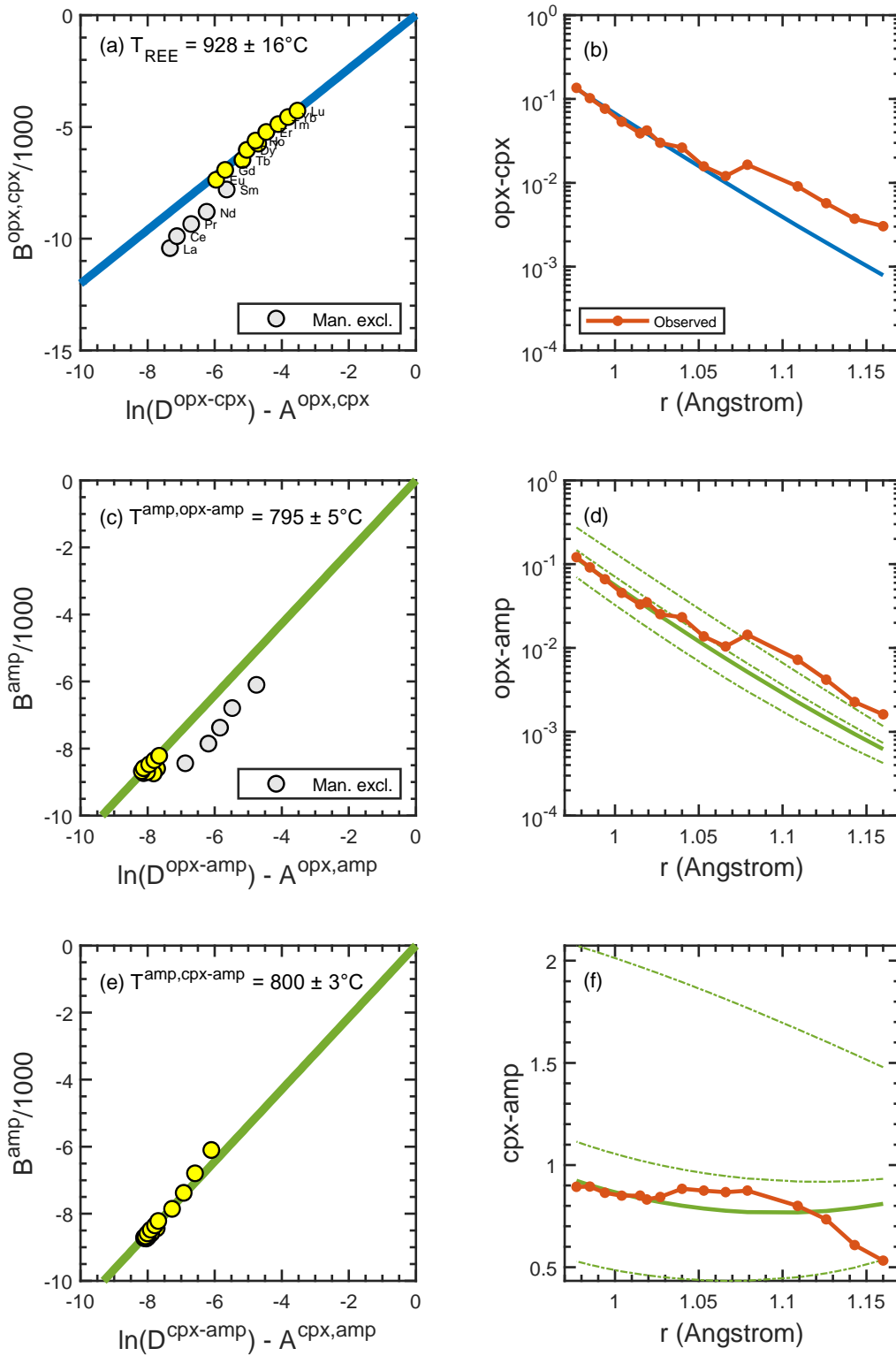


Fig. S4. Nyos3, Nyos Lakes, Cameroon, Pinter et al. (2015)

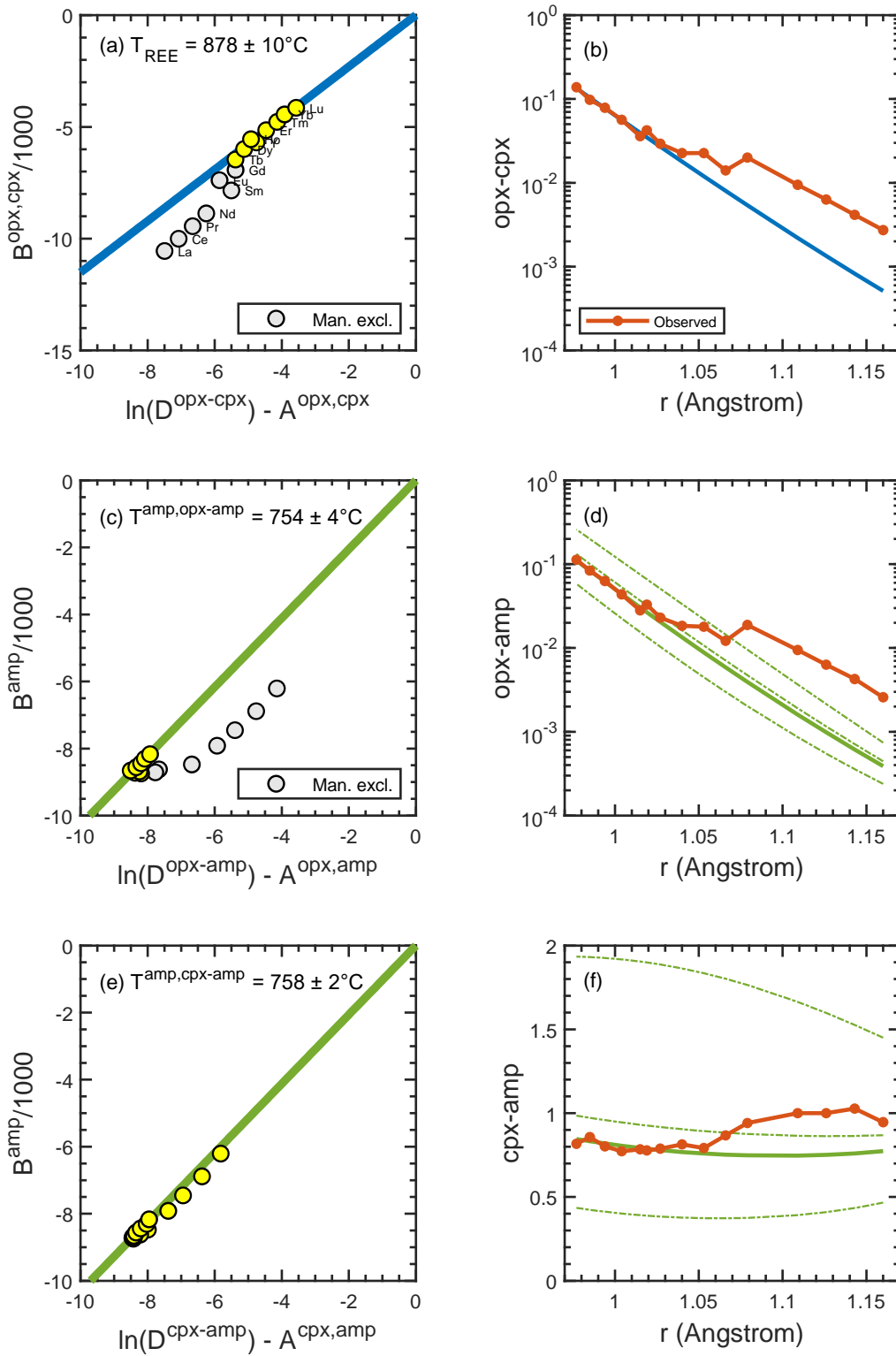


Fig. S5. WLK30, Wilcza Góra, SW Poland, Matusiak-Malek et al. (2017)

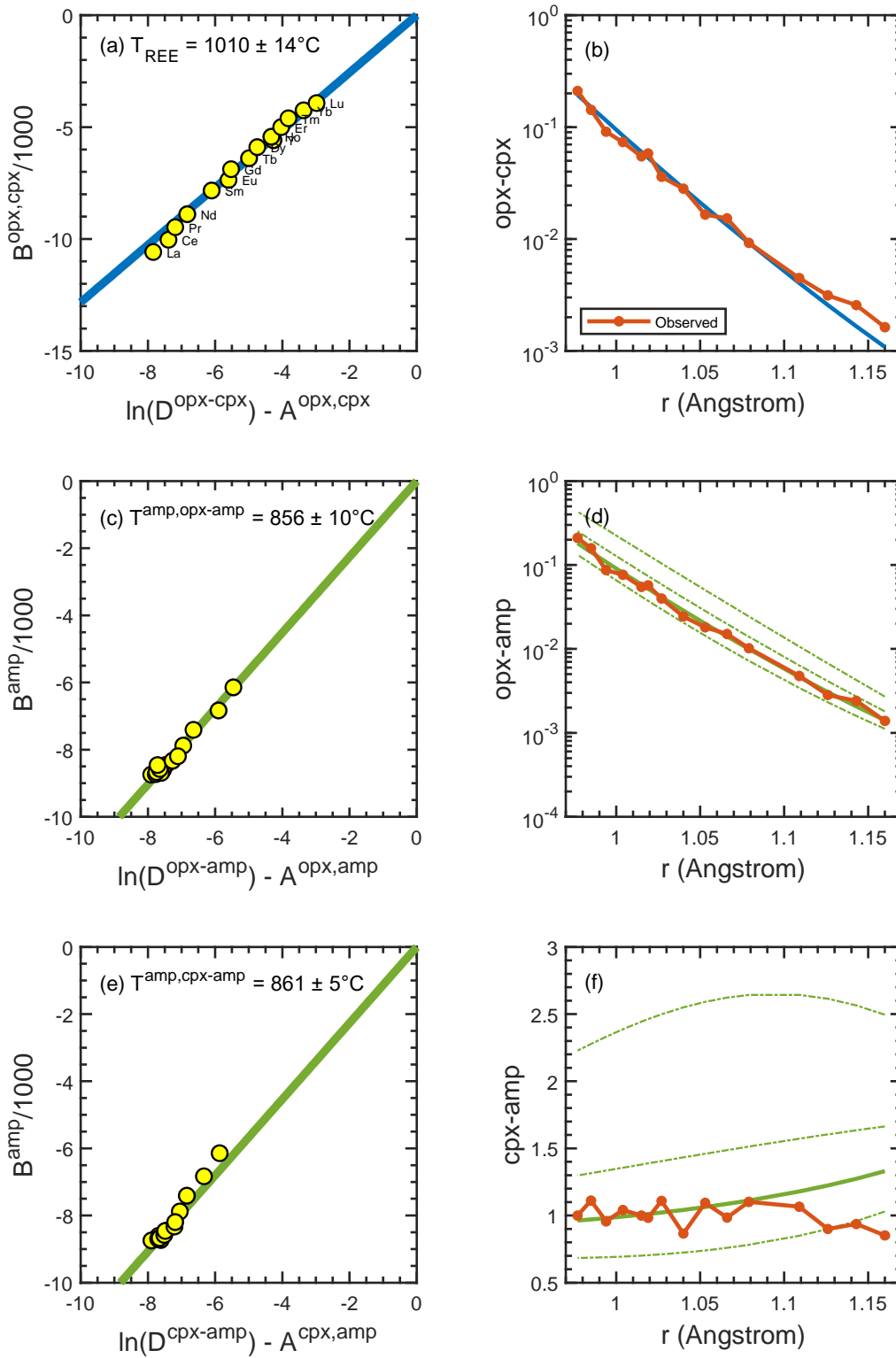


Fig. S6. AUB1407, Western Pannonian Basin, Hungary, Aradi et al. (2020)

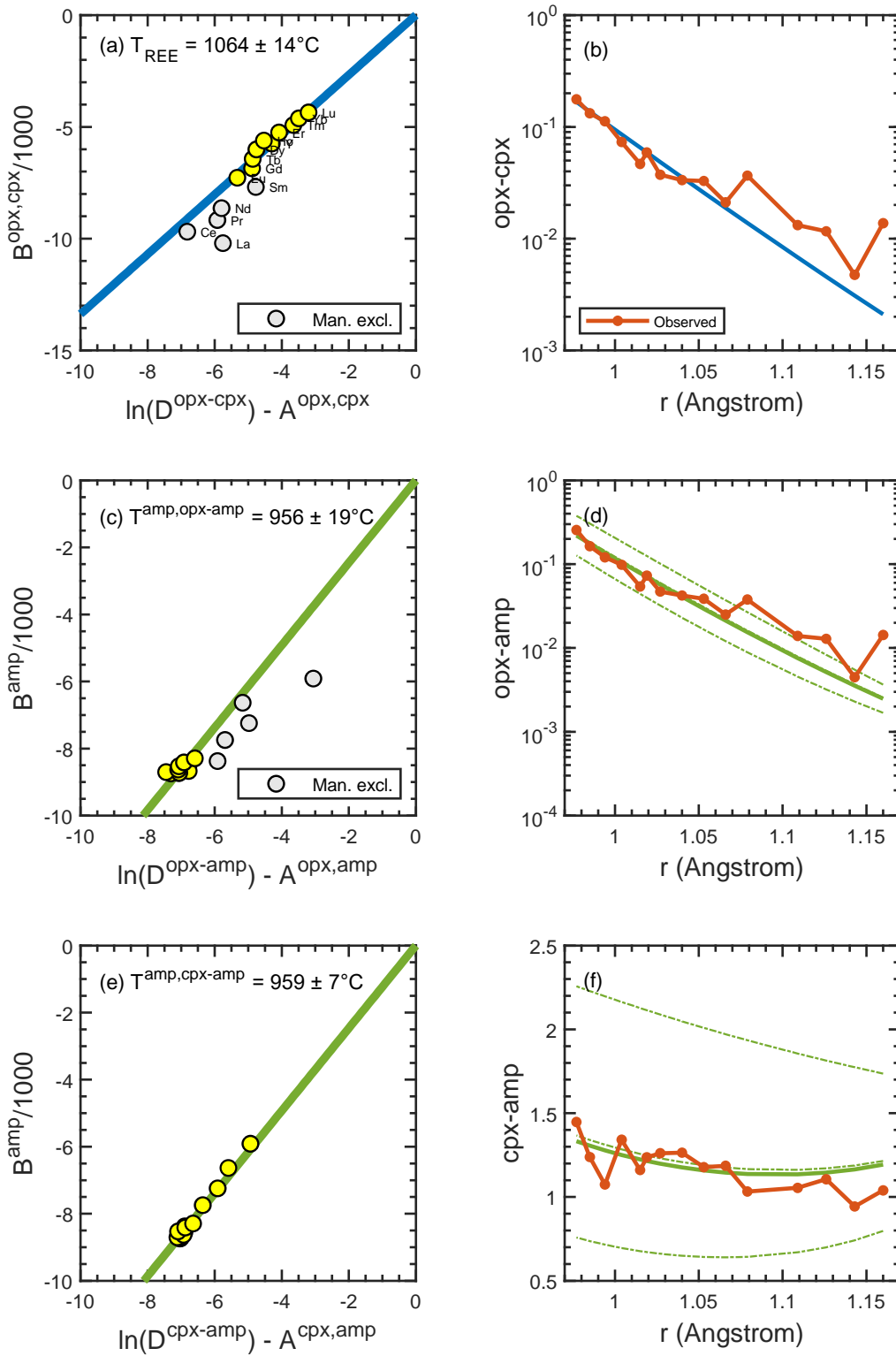


Fig. S7. AUB1410, Western Pannonian Basin, Hungary, Aradi et al. (2020)

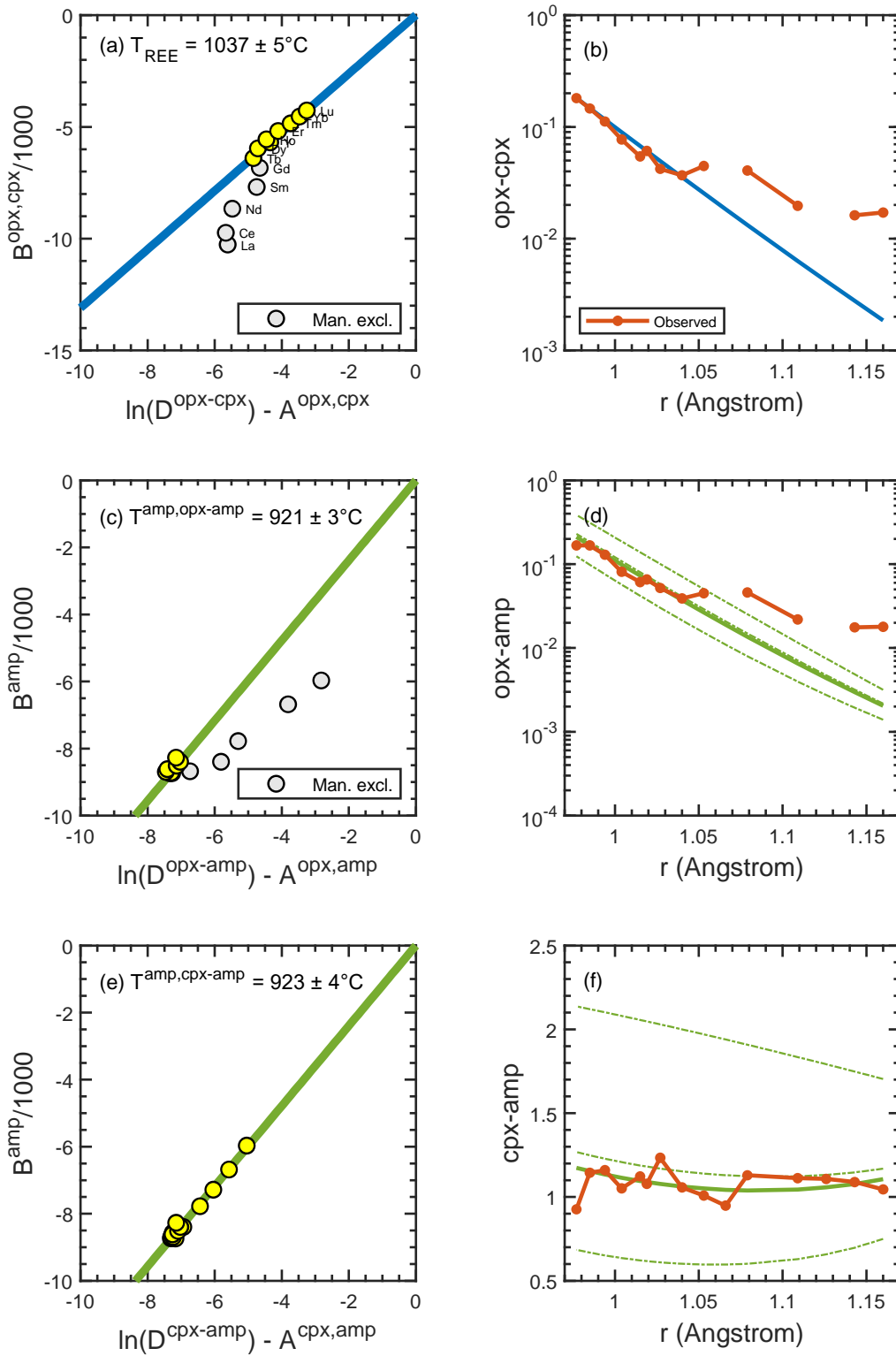


Fig. S8. BE11404, Western Pannonian Basin, Hungary, Aradi et al. (2020)

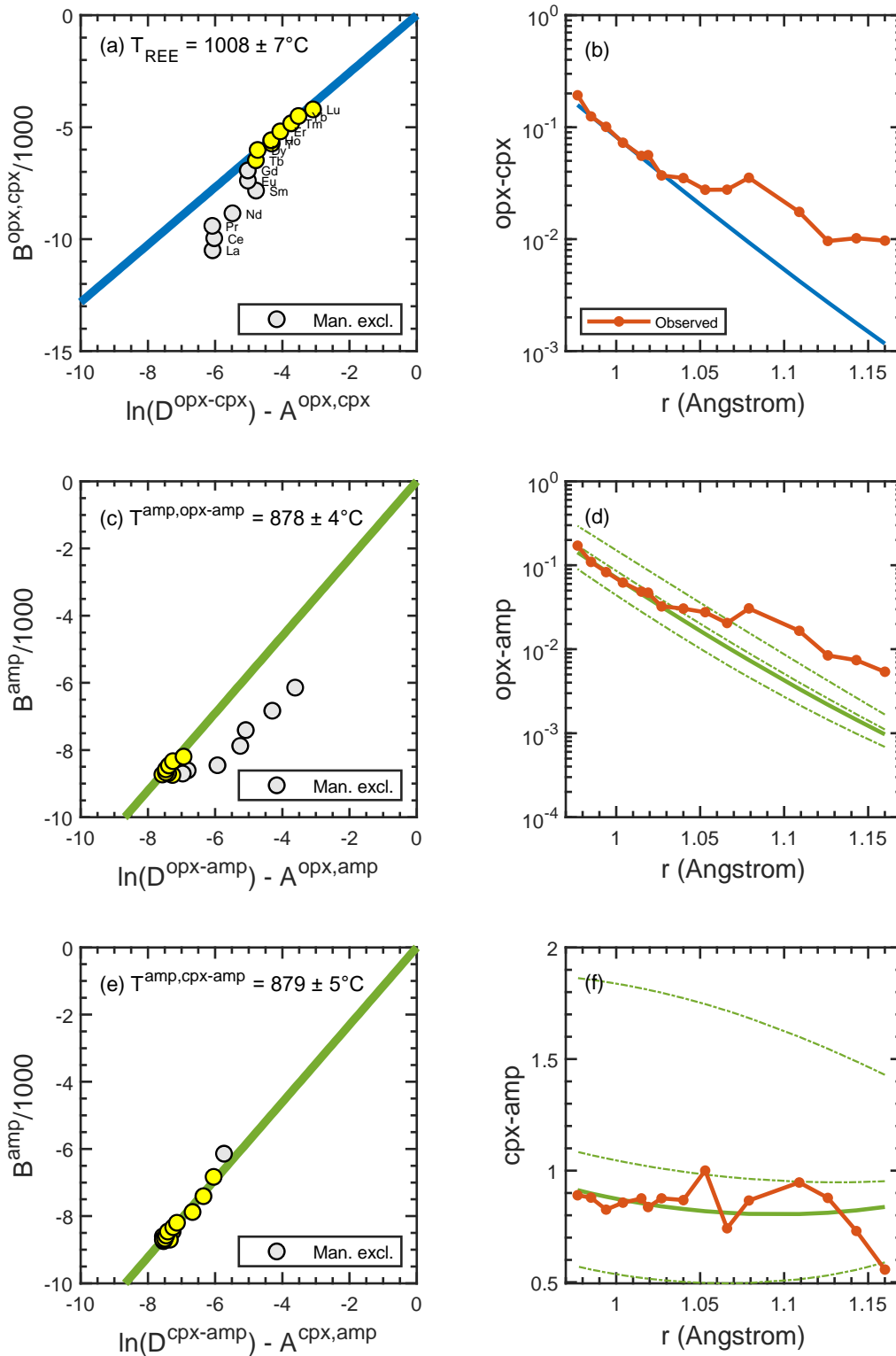


Fig. S9. FKG1402, Western Pannonian Basin, Hungary, Aradi et al. (2020)

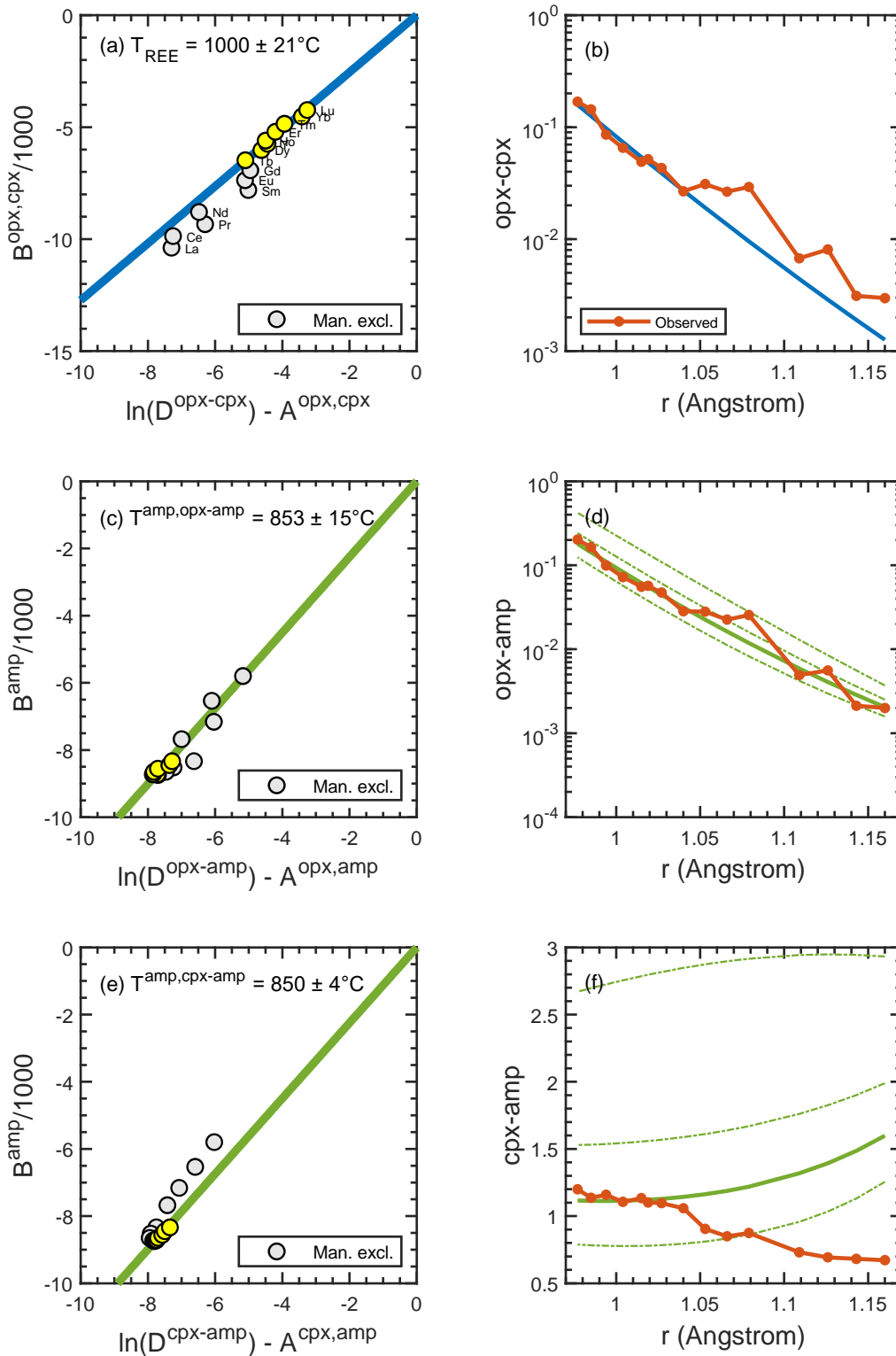


Fig. S10. GN1401, Western Pannonian Basin, Hungary, Aradi et al. (2020)

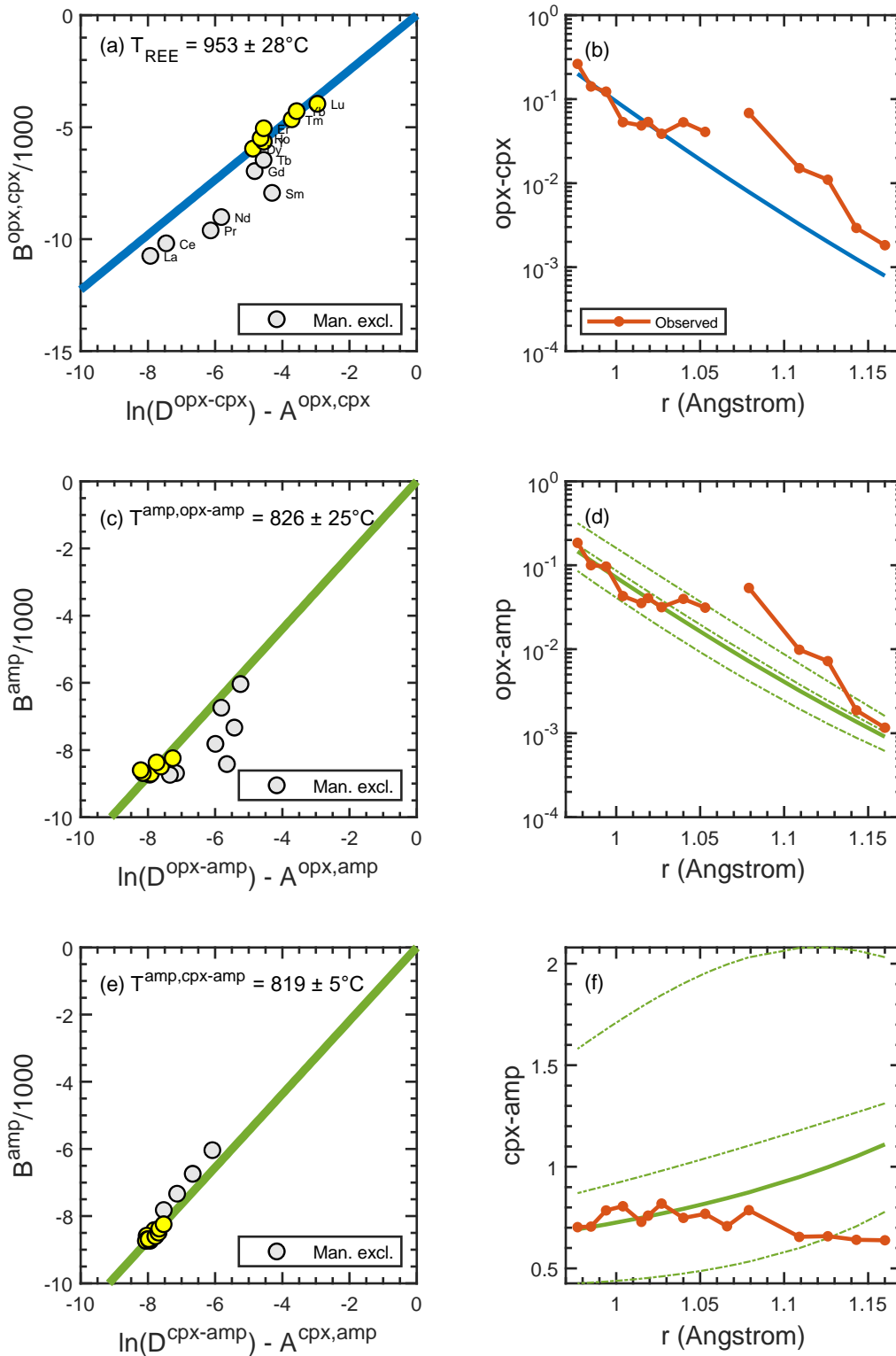


Fig. S11. GN1402, Western Pannonian Basin, Hungary, Aradi et al. (2020)

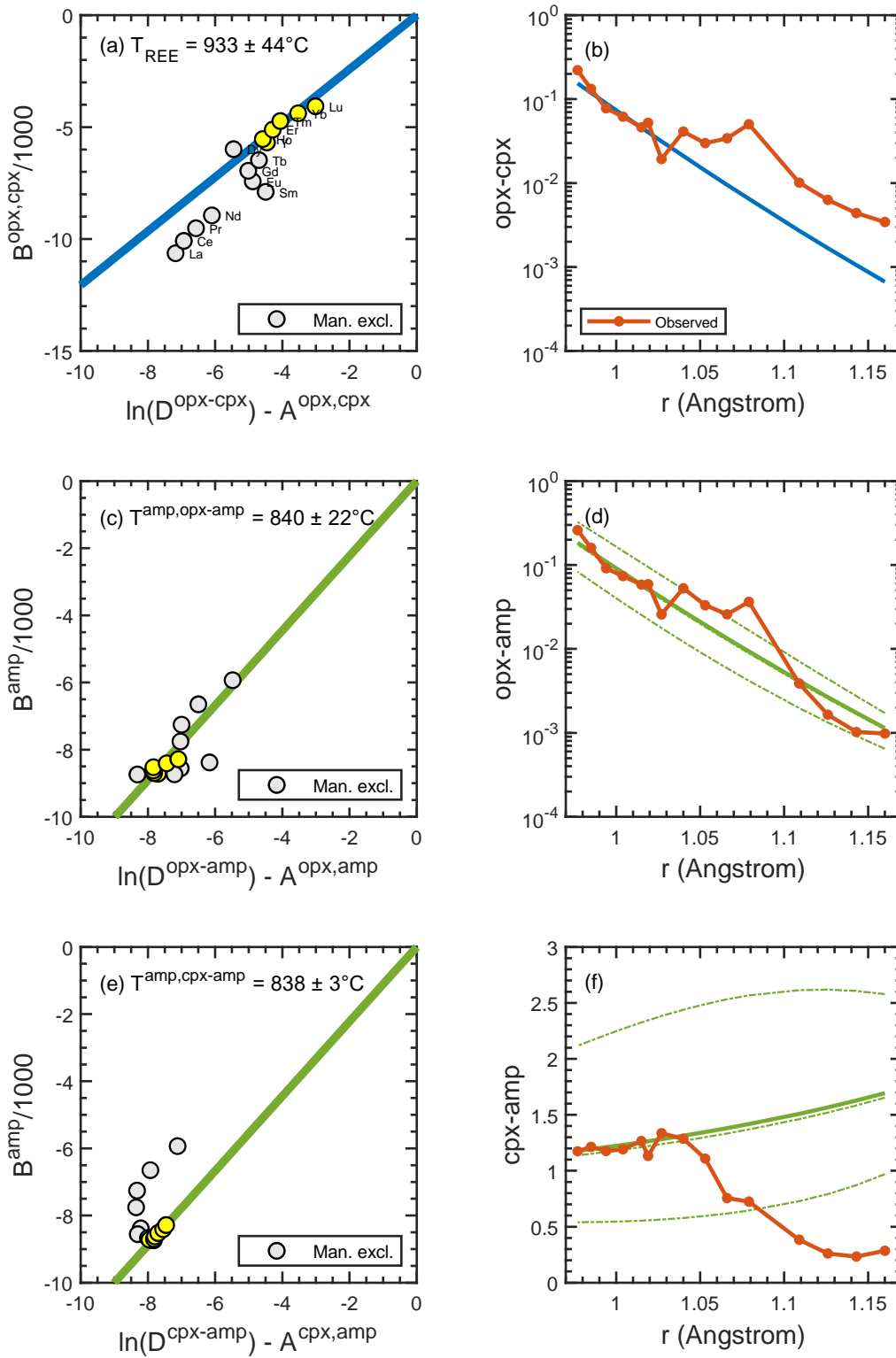


Fig. S12. GN1406, Western Pannonian Basin, Hungary, Aradi et al. (2020)

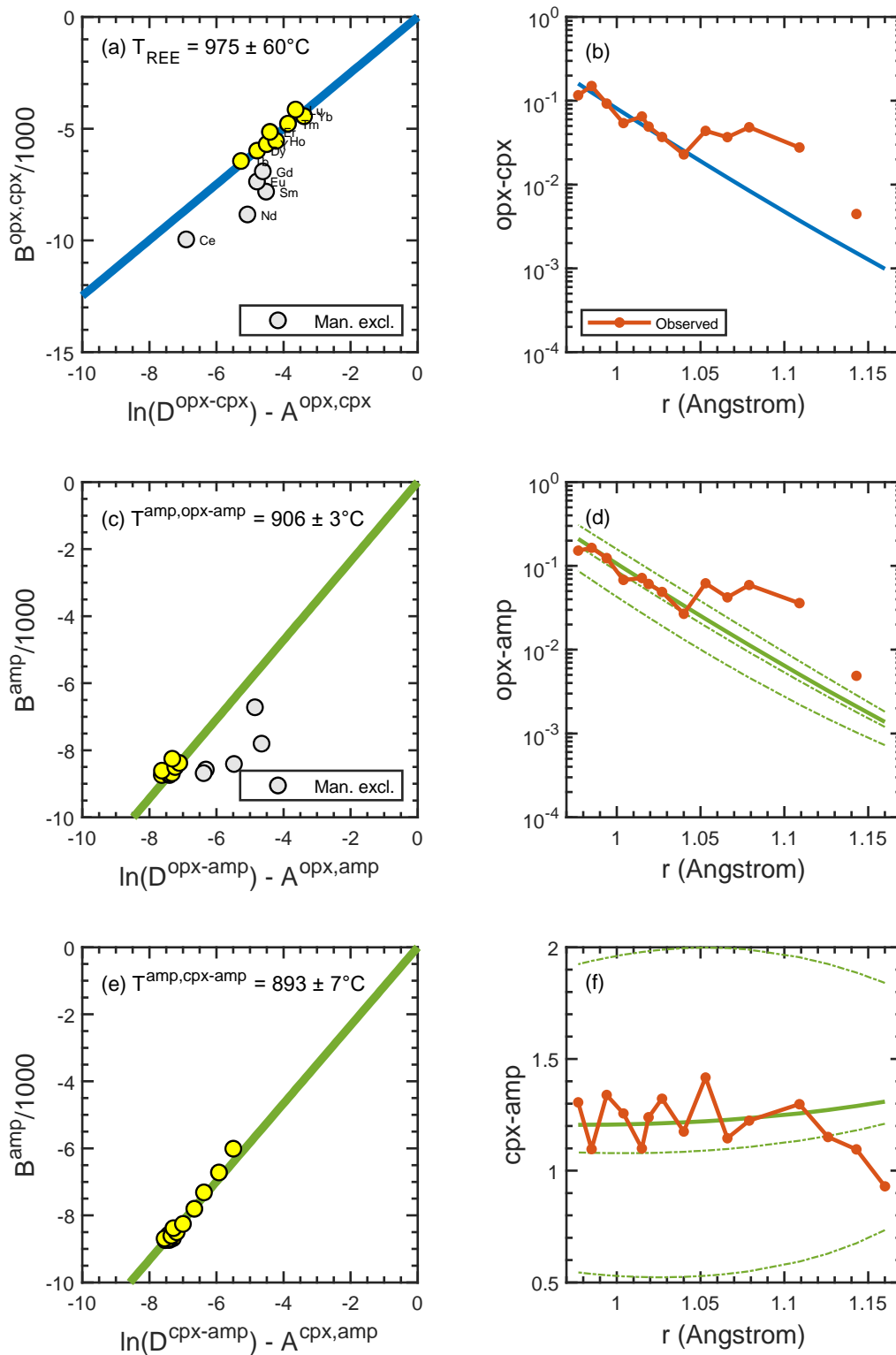


Fig. S13. GN1411, Western Pannonian Basin, Hungary, Aradi et al. (2020)

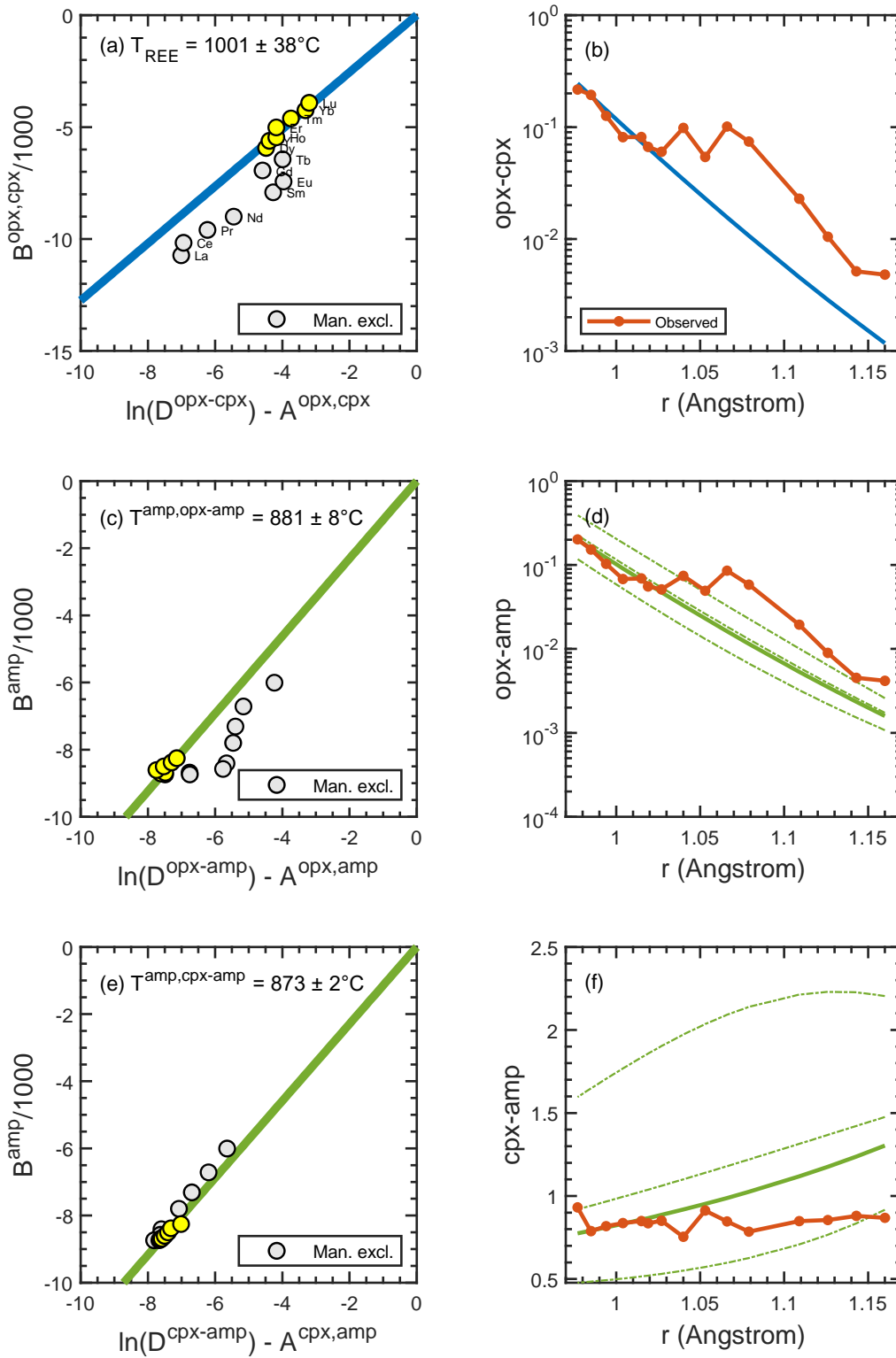


Fig. S14. GN1412, Western Pannonian Basin, Hungary, Aradi et al. (2020)

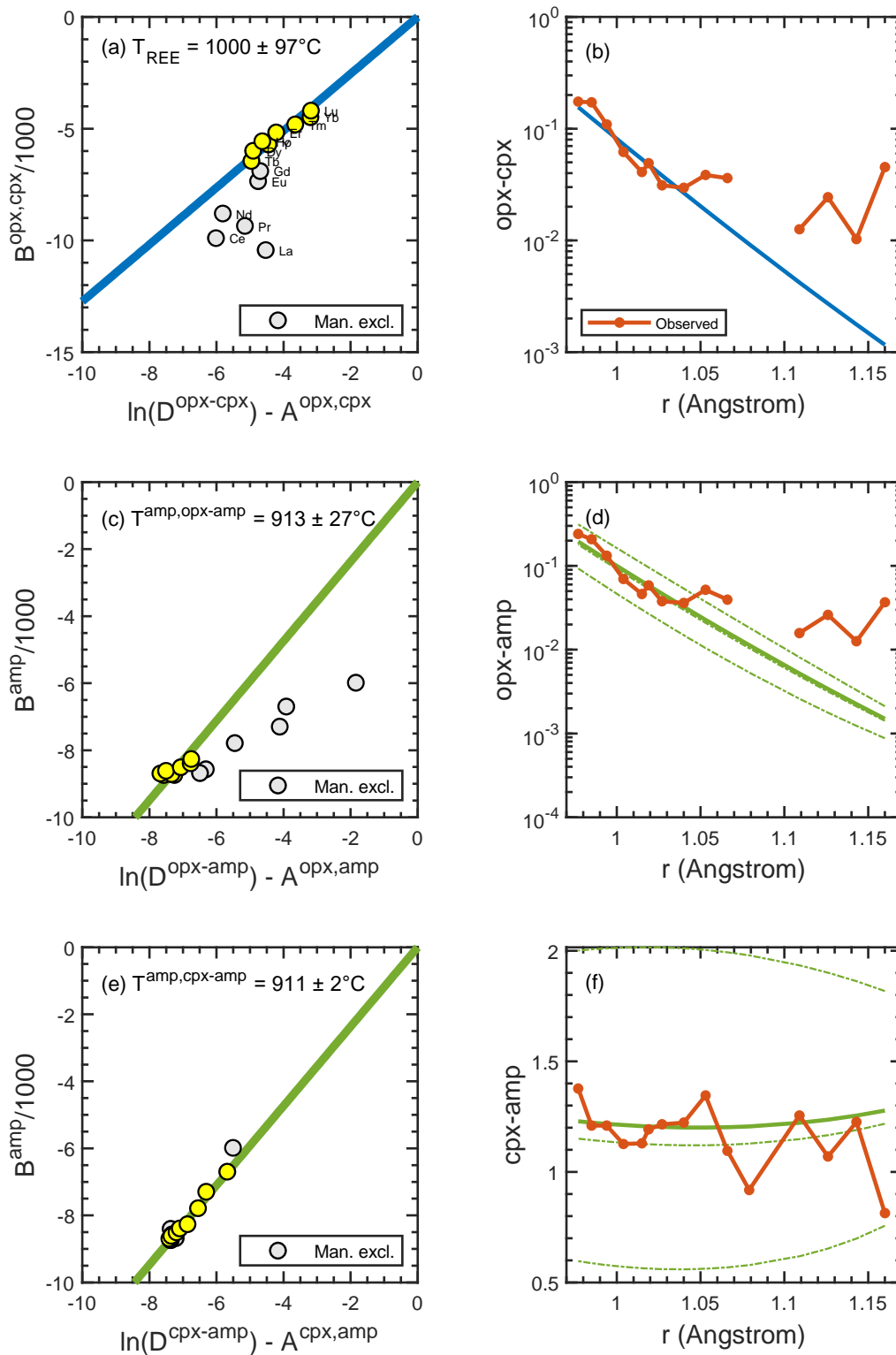


Fig. S15. NH1402, Western Pannonian Basin, Hungary, Aradi et al. (2020)

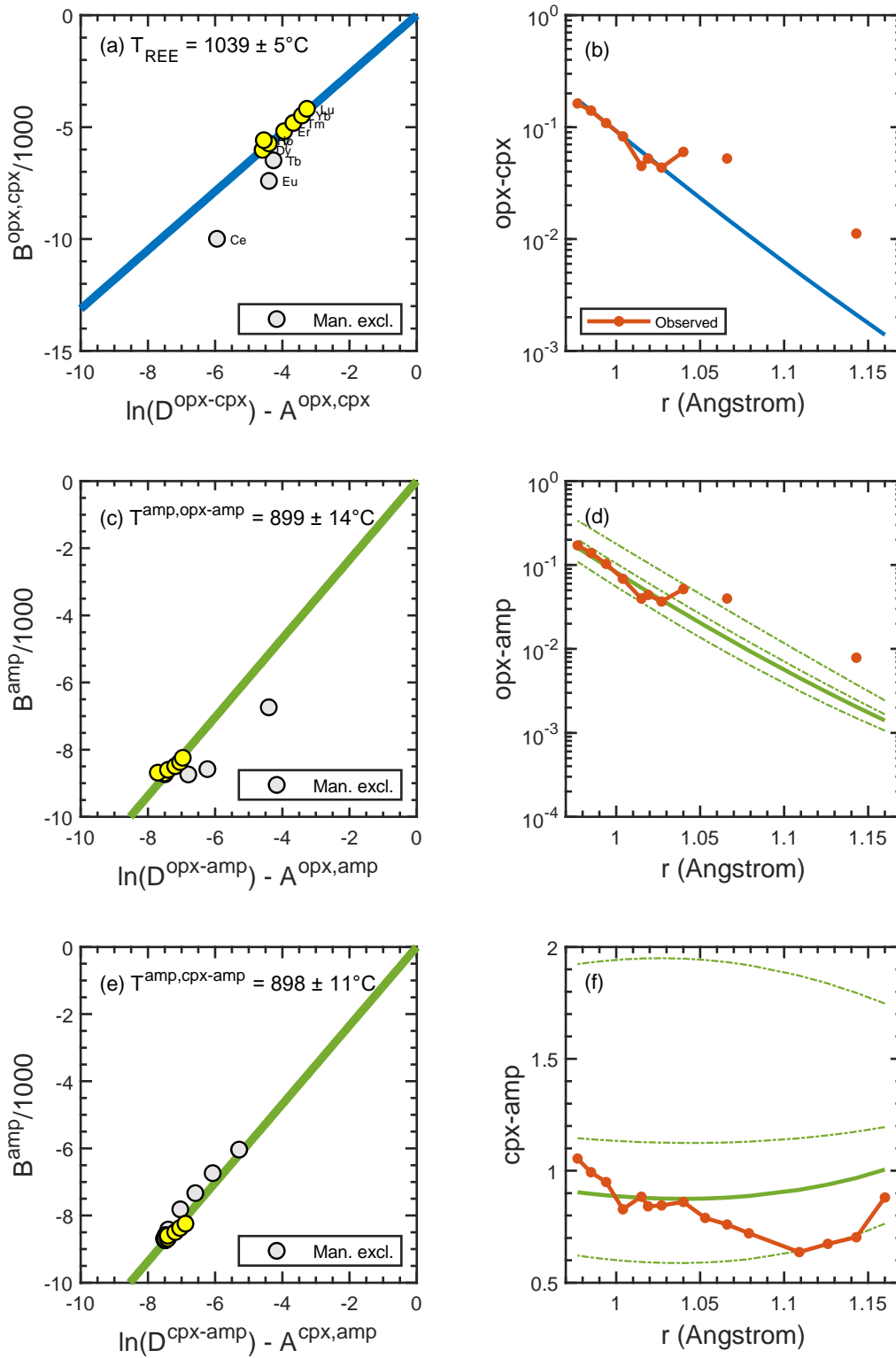


Fig. S16. NH1408, Western Pannonian Basin, Hungary, Aradi et al. (2020)

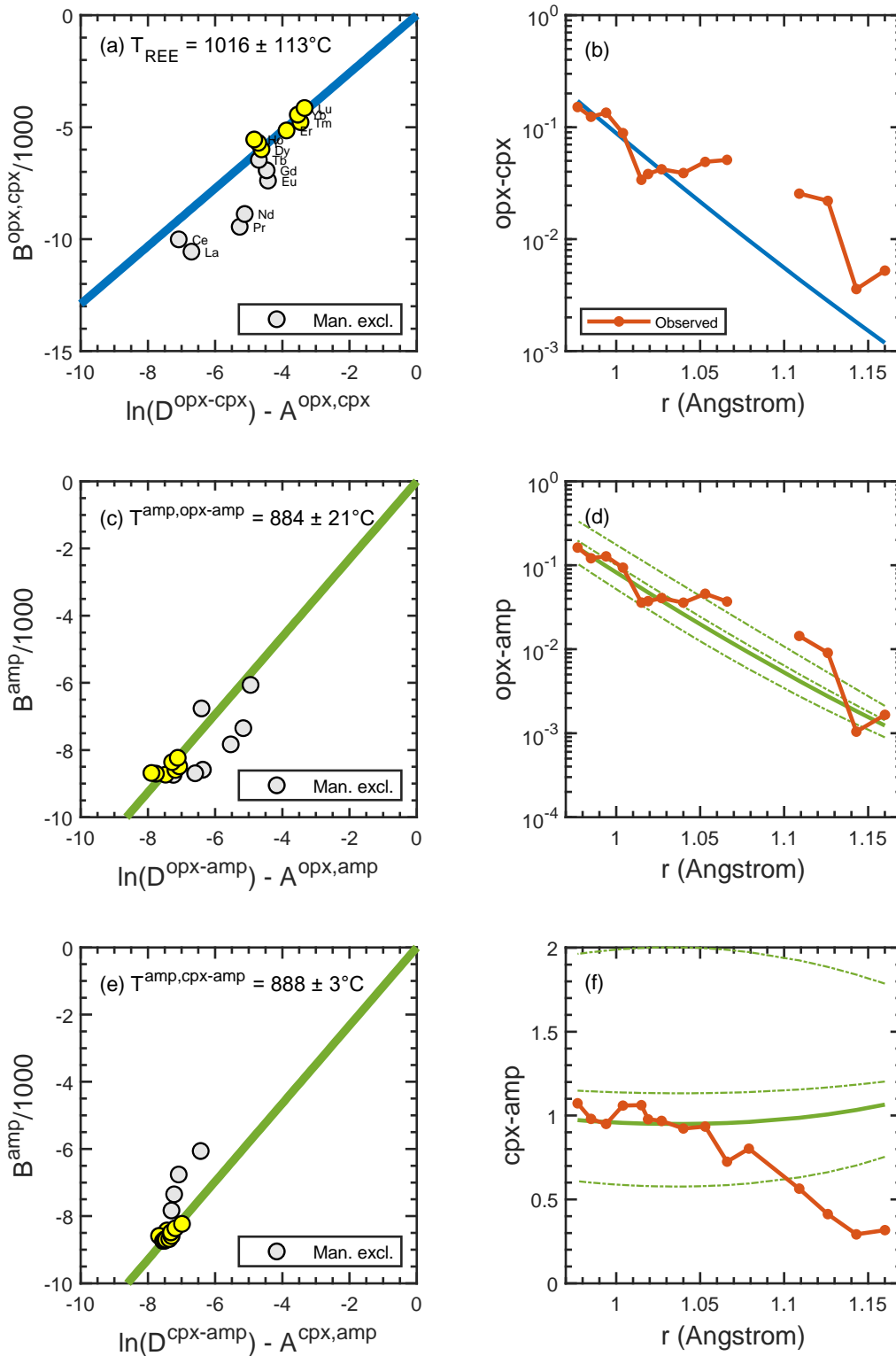


Fig. S17. RGB1416, Western Pannonian Basin, Hungary, Aradi et al. (2020)

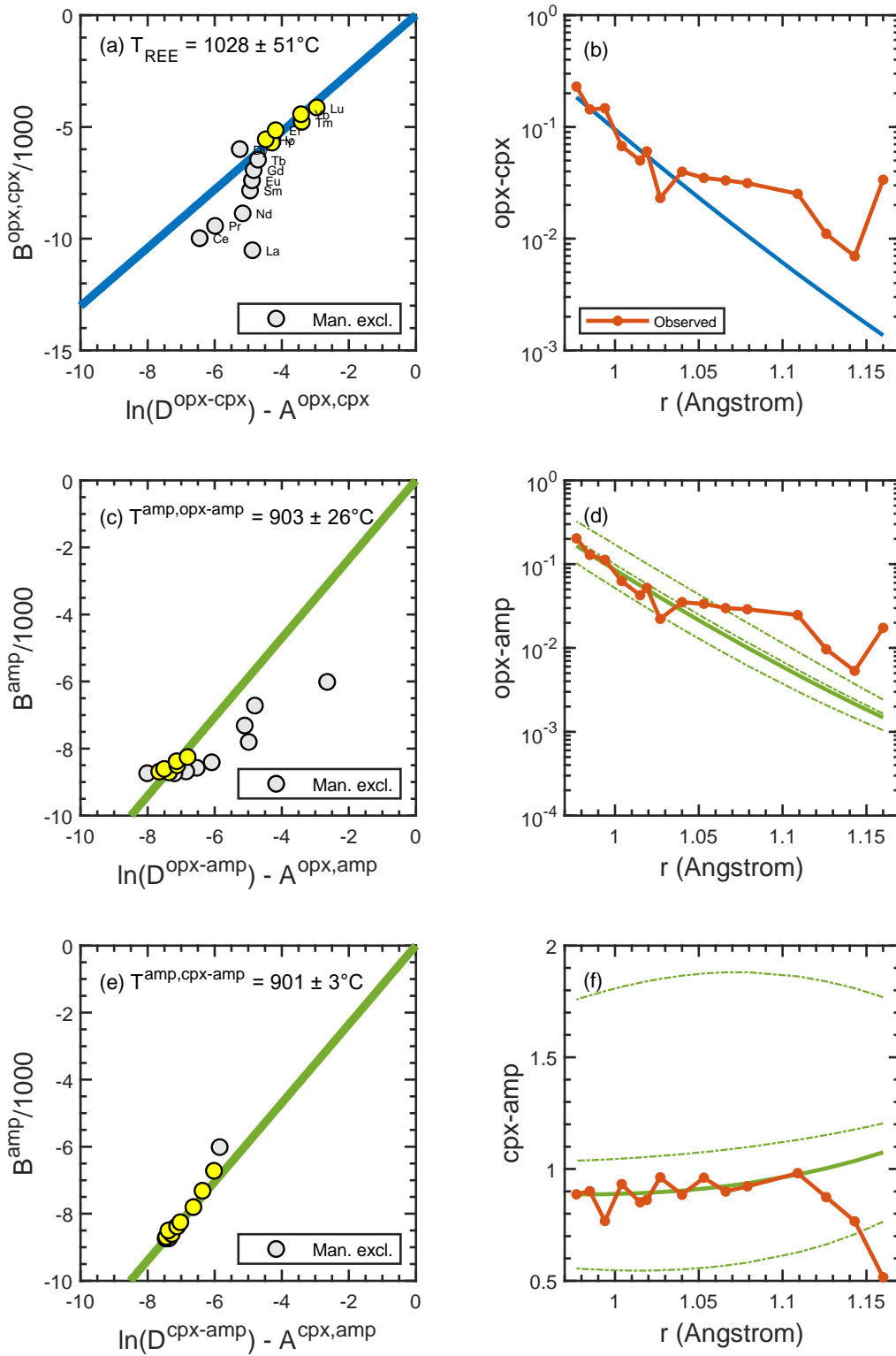


Fig. S18. RGB1454, Western Pannonian Basin, Hungary, Aradi et al. (2020)

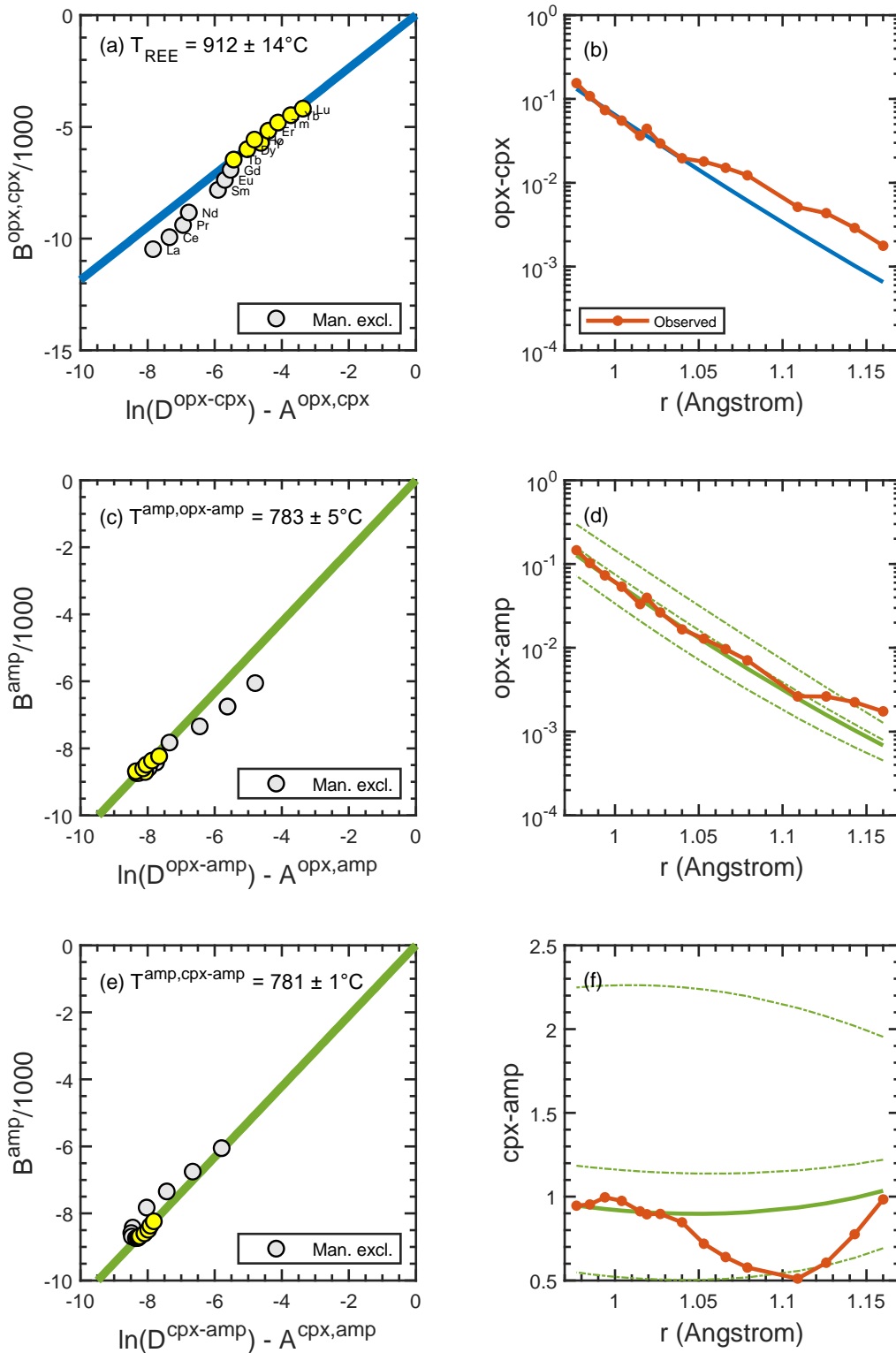


Fig. S19. SBF1401, Western Pannonian Basin, Hungary, Aradi et al. (2020)

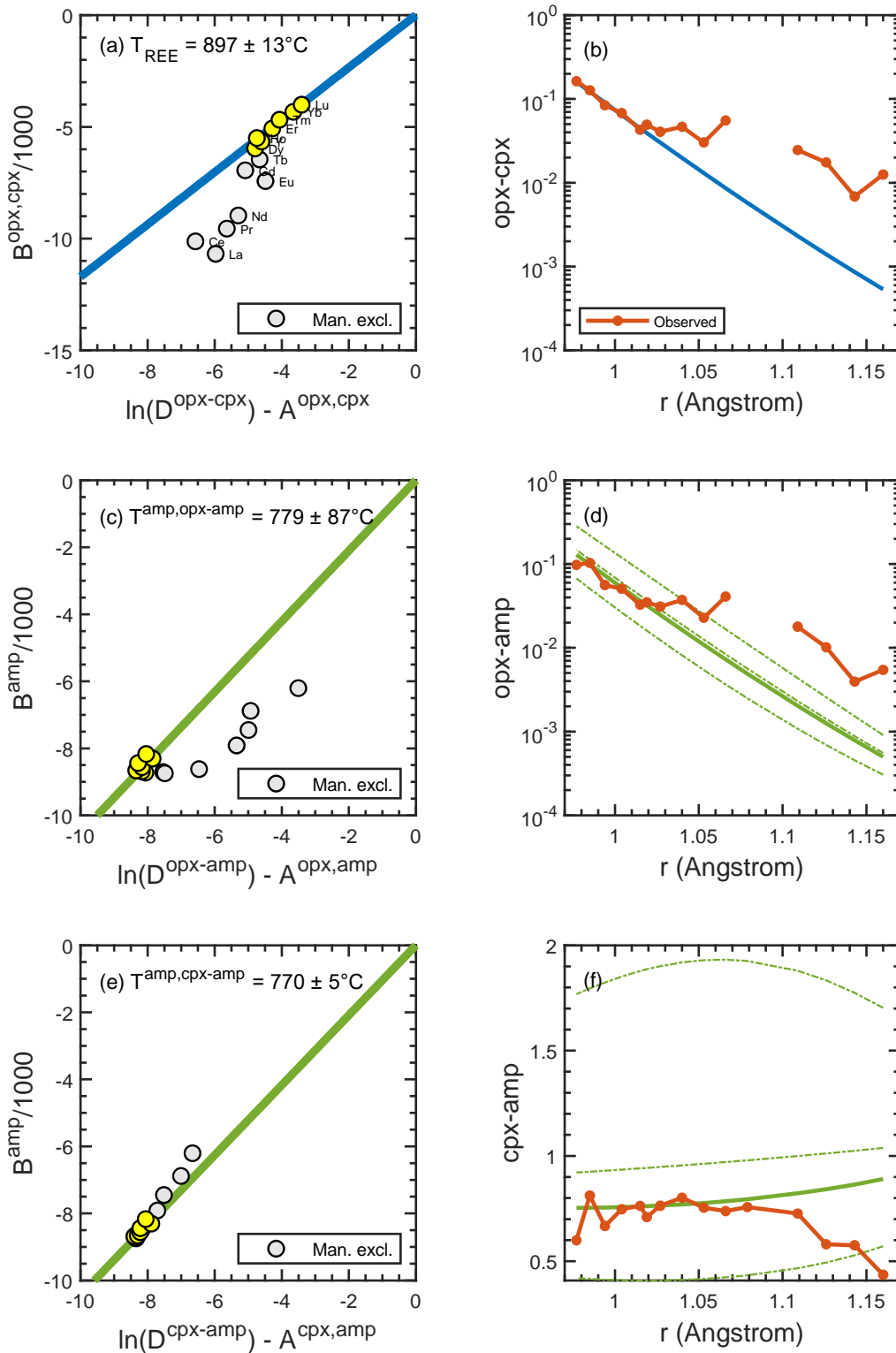


Fig. S20. TOB1401, Western Pannonian Basin, Hungary, Aradi et al. (2020)

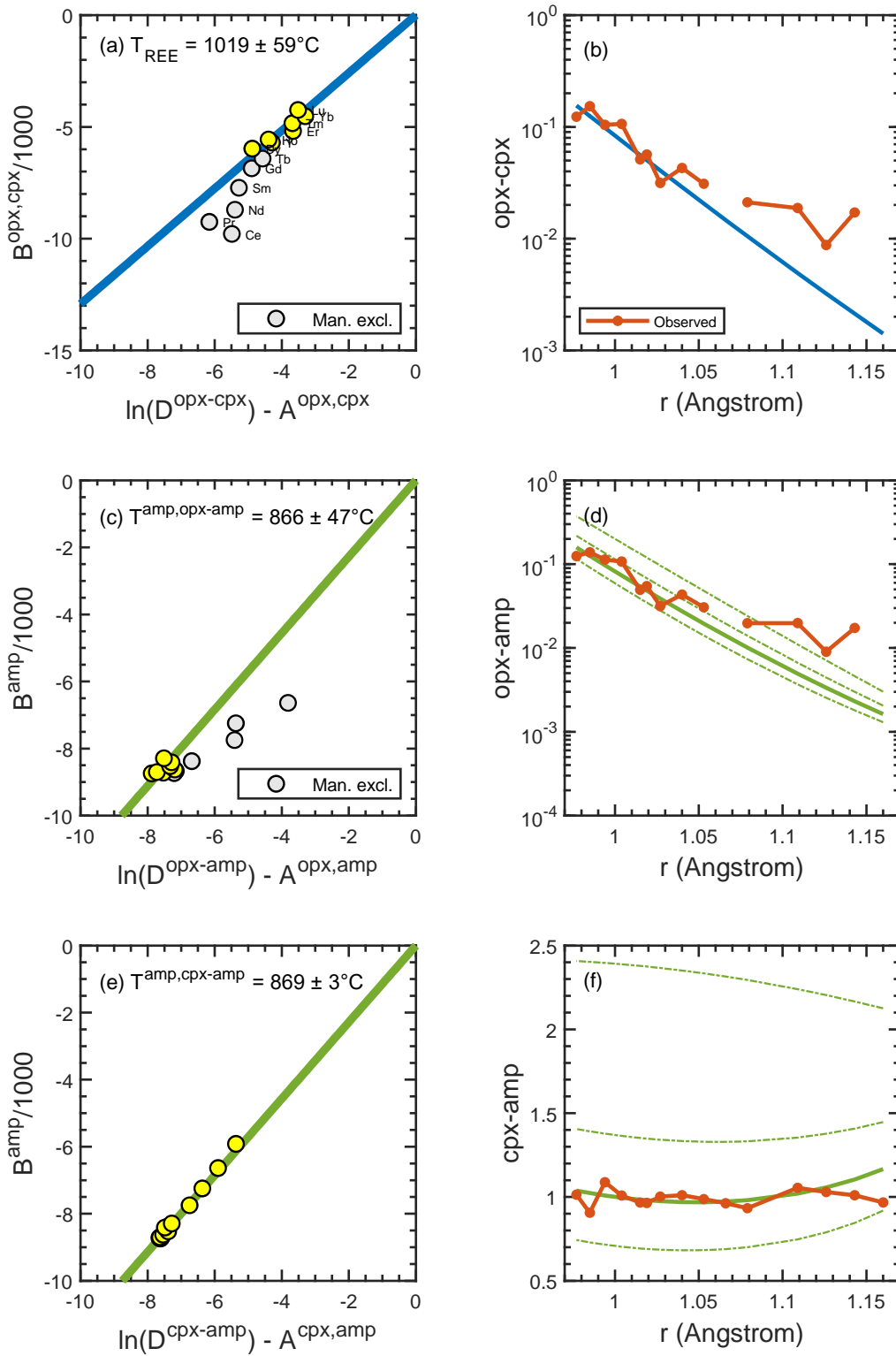


Fig. S21. TOB1403, Western Pannonian Basin, Hungary, Aradi et al. (2020)

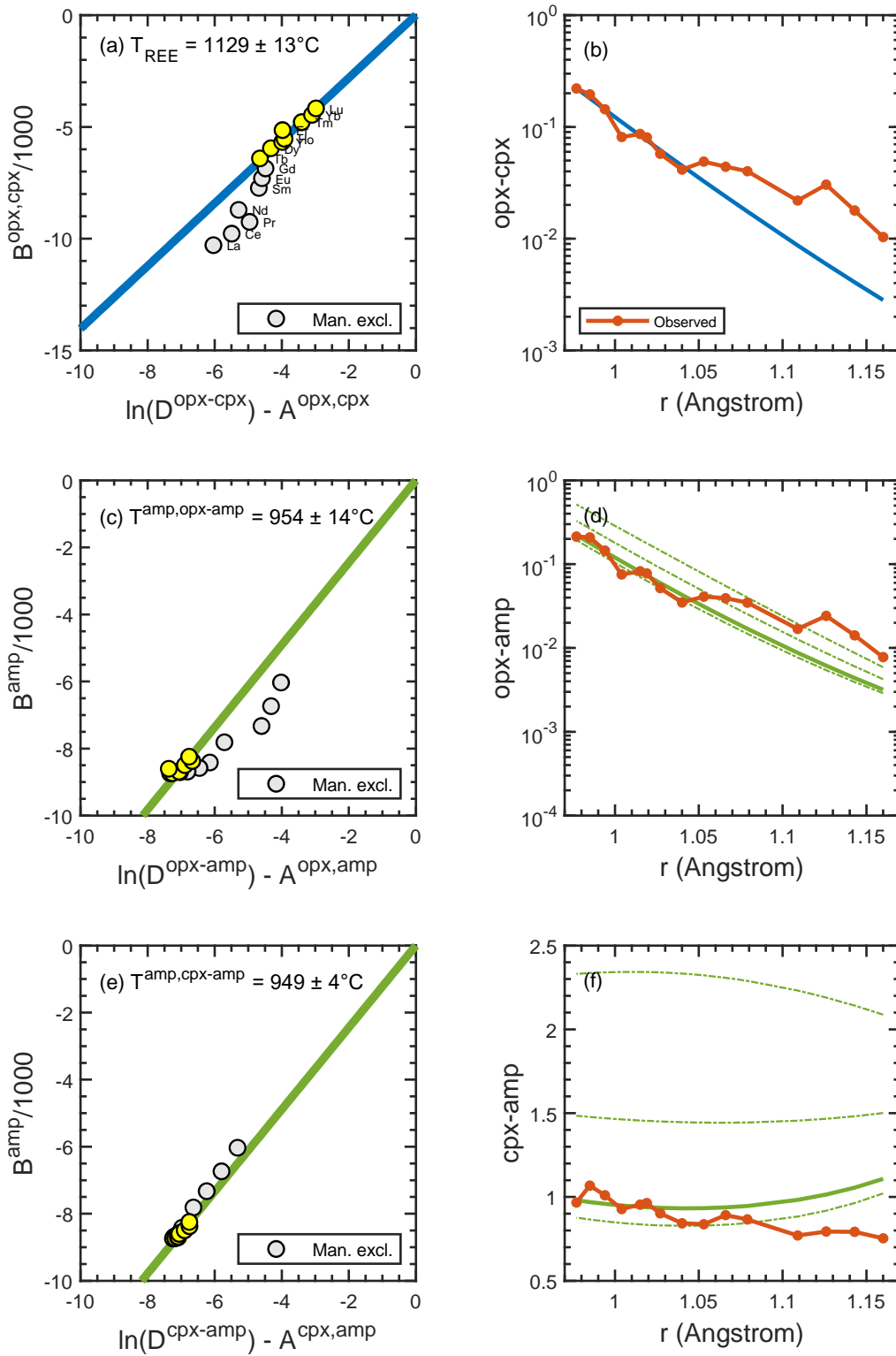


Fig. S22. 17XJ6-3, Huadian, China, Xu (Unpublished)

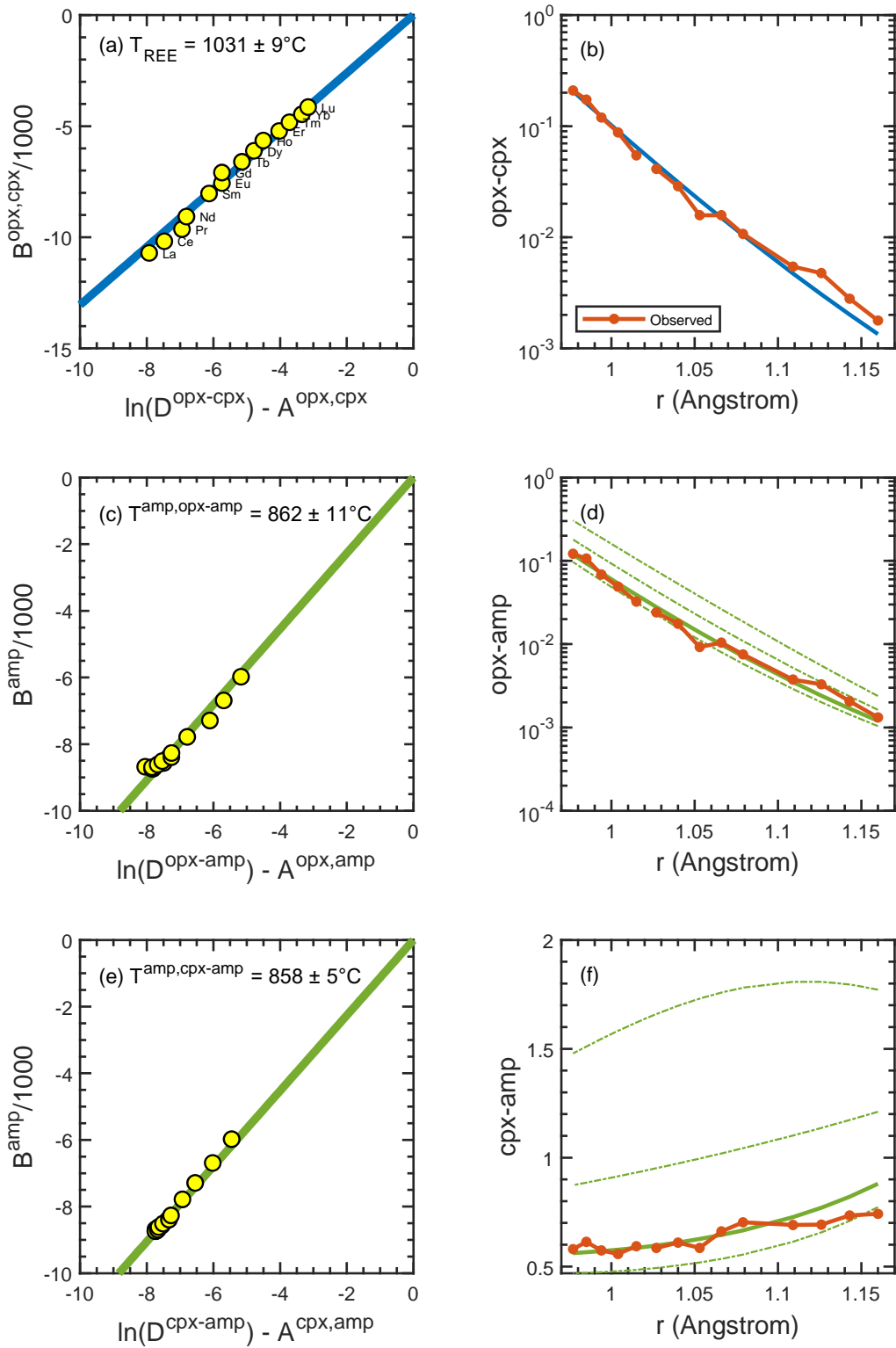


Fig. S23. BE1401, Western Pannonian Basin, Hungary, Aradi et al. (2020)

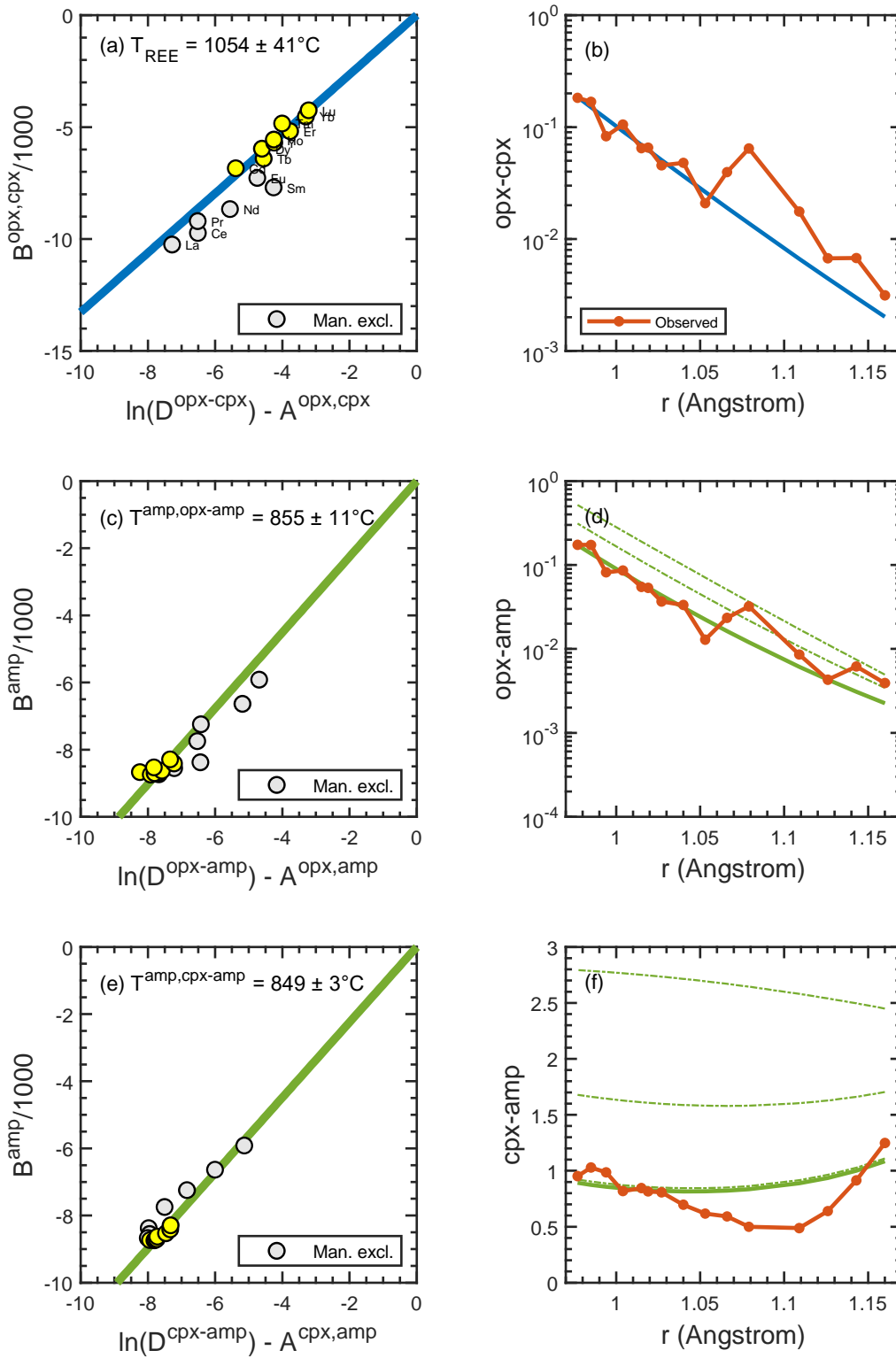
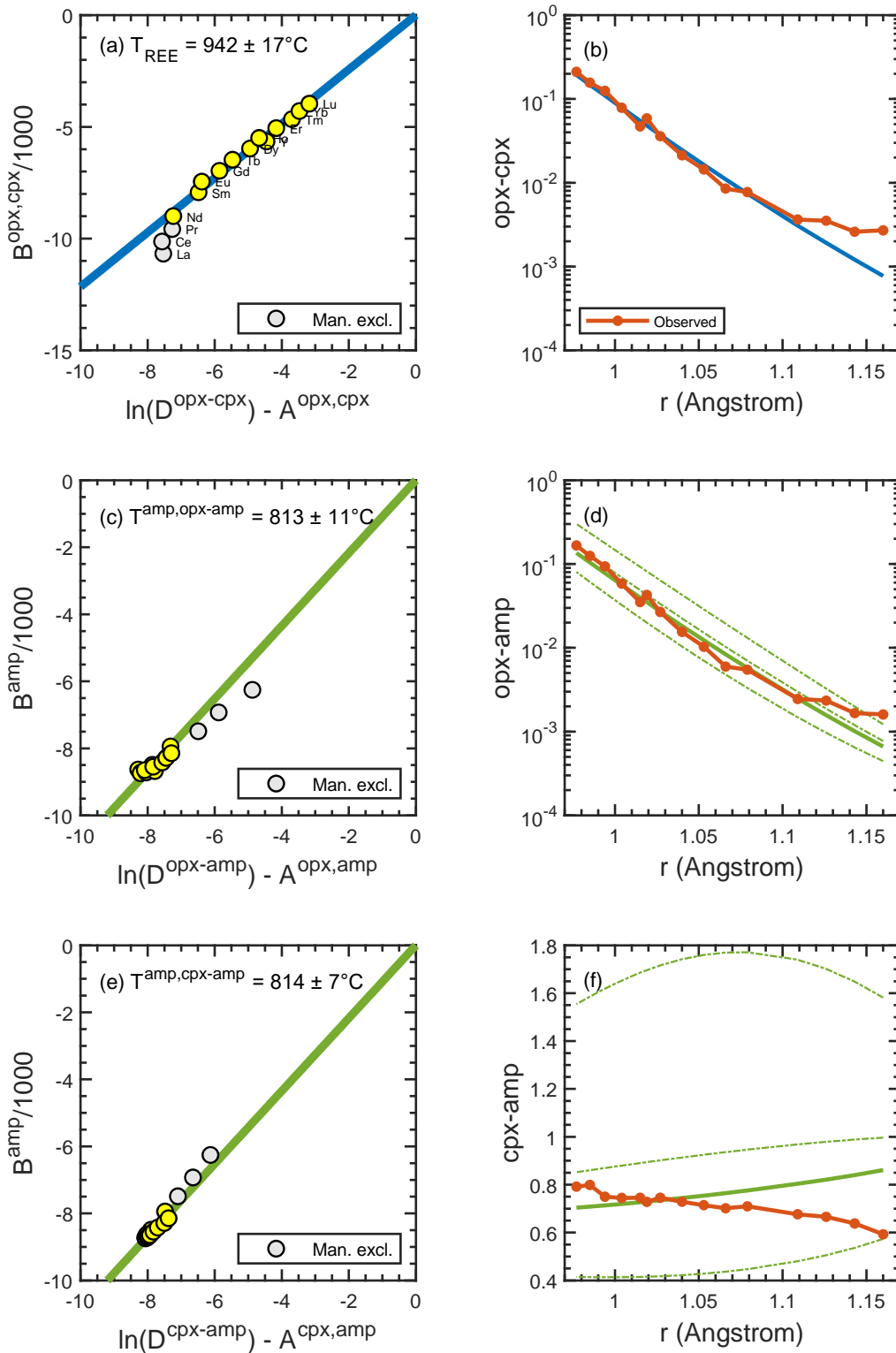


Fig. S24. MM110, Wilcza Góra, SW Poland, Matusiak-Malek et al. (2017)



## References

- Aradi, L.E., Bali, E., Patkó, L., Hidas, K., Kovács, I.J., Zanetti, A., Garrido, C.J., and Szabo, C. (2020) Geochemical evolution of the lithospheric mantle beneath the Styrian Basin (Western Pannonian Basin). *Lithos*, 378–379, 105831.
- Brey, G.P., Köhler, T. (1990) Geothermobarometry in four-phase lherzolites II. New thermobarometers, and practical assessment of existing thermobarometers. *Journal of Petrology*, 31, 1353–1378.
- Gregoire, M., Lorand, J.P., O'Reilly, S.Y., and Cottin, J.Y. (2000) Armalcolite-bearing, Ti-rich metasomatic assemblages in harzburgitic xenoliths from the Kerguelen Islands: implications for the oceanic mantle budget of high-field strength elements. *Geochimica et Cosmochimica Acta*, 64, 673–694.
- Hawthorne, F.C. (1983) The crystal chemistry of the amphiboles. *Canadian Mineralogist*, 2, 173–480.
- Leake, B.E., Woolley, A.R., Arps, C.E.S., Birch, W.D., Gilbert, M.C., Grice, J.D., Hawthorne, F.C., Kato, A., Kisch, H.J., Krivovichev, V.G., and others. (1997) Nomenclature of amphiboles: report of the subcommittee on amphiboles of the International Mineralogical Association, Commission on New Minerals and Mineral Names. *Canadian Mineralogist*, 35, 219–246.
- Liang, Y., Sun, C., and Yao, L. (2013) A REE-in-two-pyroxene thermometer for mafic and ultramafic rocks. *Geochimica et Cosmochimica Acta*, 102, 246–260.
- Matusiak-Małek, M., Puziewicz, J., Ntaflos, T., Grégoire, M., Kukuła, A., and Wojtulek, P.M. (2017) Origin and evolution of rare amphibole-bearing mantle peridotites from Wilcza Góra (SW Poland), Central Europe. *Lithos*, 286–287, 302–323.
- Pintér, Z., Patkó, L., Djoukam, J.F.T., Kovács, I., Tchouankoue, J.P., Falus, G., Konc, Z., Tommasi, A., Barou, F., Mihály, J., Németh, C., and Jeffries, T. (2015) Characterization of the sub-continental lithospheric mantle beneath the Cameron volcanic line inferred from alkaline basalt hosted peridotite xenoliths from Barombi Mbo and Nyos Lakes. *Journal of African Earth Sciences*, 111, 170–193.
- Shimizu, K., Sun, C., Liang, Y., Jackson, C.R.M., and Saal, A.E. (2017) Parameterized lattice strain models for REE partitioning between amphibole and silicate melt. *American Mineralogist*, 102, 2254–2267.

- Witt-Eickschen, G., and Harte, B. (1994) Distribution of trace elements between amphibole and clinopyroxene from mantle peridotites of the Eifel (western Germany): An ion-microprobe study. *Chemical Geology*, 117, 235–250.
- Witt-Eickschen, G., and O'Neill, H.S.C. (2005) The effect of temperature on the equilibrium distribution of trace elements between clinopyroxene, orthopyroxene, olivine and spinel in upper mantle peridotite. *Chemical Geology*, 221, 65–101.
- Zhou, Q. (2014) Petrogenesis of wehrlite and pyroxenite xenoliths in early Cretaceous igneous Rocks from western Shandong, China. (Ph.D. Thesis), Jilin University, Changchun (in Chinese with English abstract).